Adaptive Grid Refinement for High-Order Finite Volume Simulations of Unsteady Compressible and Turbulent Flows

Ariadni Liapi, Mikail Salihoglu, Anca-Claudia Belme, Pierre Brenner, Alexandre Limare, Gregoire Pont, Paola Cinnella

Adaptive Grid Refinement for High-Order Finite Volume Simulations of Unsteady Compressible and Turbulent Flows

Ariadni Liapi[a,*], Mikail Salihoglu[a], Anca-Claudia Belme[a], Pierre Brenner[b], Alexandre Limare[b], Gregoire Pont[c], Paola Cinnella[a]

[a] *Institut Jean Le Rond d'Alembert, Sorbonne Université, 75005, Paris, France*
[b] *ArianeGroup, 66 Rte de Verneuil, 78130 Les Mureaux, France*
[c] *Airbus SAS, 31 Rue des Cosmonautes, 31400 Toulouse, France*

Abstract

This study investigates dynamic mesh adaptation (DMA) for hybrid RANS/LES (HRLES) simulations of compressible turbulent flows. HRLES models, which blend Reynolds-Averaged Navier–Stokes (RANS) and Large Eddy Simulation (LES), are by their nature very sensitive to the computational mesh, because of the very different resolution requirements in the RANS and LES regions. The proposed DMA strategy relies on a high-order k-exact finite volume spatial discretization [1] designed to ensure robust, accurate and conservative solutions for compressible flows with strong discontinuities while limiting the numerical dissipation of vortical structures. A mesh refinement criterion related to the truncation error of the k-exact reconstruction scheme is introduced, and compared with several heuristic refinement criteria from the literature. To limit the computational burden of frequent re-meshing for unsteady flow simulations, the adaptation is performed only at certain time steps, and the error criterion is averaged over the chosen adaptation period. A simple and effective criterion is then introduced to automatically control the adaptation period. The proposed DMA strategy is evaluated against a series of test cases of increasing complexity, ranging from inviscid vortex advection to turbulent transonic flow past an axisymmetric backward-facing step, representative of the base flow behind a space launcher.

Keywords: Adaptive Mesh Refinement, RANS/LES, compressible flows, k-exact Finite Volume scheme, Mean refinement criteria

*Corresponding author
Email address: ariadni.liapi@dalembert.upmc.fr (Ariadni Liapi)

1. Introduction

Hybrid RANS/LES simulations (HRLES), which combine the Reynolds-Averaged Navier–Stokes (RANS) and the Large Eddy Simulation (LES) models to describe unsteady turbulent flows, have gained increasing interest for industrial applications. HRLES methods seek for an optimal blending of the RANS and LES methods based on estimates of the characteristic turbulent scales, with the general idea of using RANS in thin, attached flow regions where RANS can provide cheap and reasonably accurate solutions, and switching to LES in regions where the flow is dominated by the unsteady dynamics of large vortical structures. While the RANS turbulent scales are generally estimated from local turbulent properties (such as the local turbulent kinetic energy and dissipation rate), the LES scale is representative of the smallest turbulent scales that can be resolved in the simulation and is then directly related to the local mesh size. Several HRLES models exist in the literature, such as the Detached Eddy Simulation (DES) originally proposed by Spalart *et al.* [2] and its subsequent variants such as the Zonal Detached Eddy Simulation (ZDES) proposed by Deck *et al.* [3], Delayed Detached Eddy Simulation (DDES) [4], Improved Delayed Detached-Eddy Simulation (IDDES) [5], as well as alternative approaches such as the Limited Numerical Scale (LNS) approach [6], Partially Averaged Navier Stokes (PANS) [7], and the resolved kinetic energy method of [8]. Because LES quality is highly sensitive to the numerical errors introduced by the discretization scheme used to approximate the governing equations and to the grid quality, RANS/LES inherits of the same sensitivities. In addition, the RANS/LES switch is also highly dependent on the design of the computational mesh [2]. The latter must be fine enough to resolve all the relevant turbulent structures in the LES regions, while minimizing the number of cells in the RANS regions and ensuring an optimal transition between the two. Despite the progress made in the last decades, such as the introduction of empirical "shielding" functions, a poorly designed mesh can lead to a catastrophic lack of accuracy [9]. On the other hand, the design of an optimal mesh for HRLES is a difficult and time-consuming task, and the development of automatic meshing approaches capable of adapting the local mesh resolution to the resolved turbulent content is highly desirable (see for instance [10]). The goal of this study is precisely to investigate mesh adaptation strategies well suited for HRLES.

Three main approaches for adapting the spatial resolution of fluid flow simulations have been considered in the literature: (i) h-adaptation, which consists in modifying the local mesh size while keeping the order of the numerical approximation constant [11, 12], (ii) p-adaptation, which varies the order of the numerical approximation while keeping the element size constant [13, 14], and (iii)

hp-adaptation, which combines *h*- and *p*-adaptation [15, 16, 17]. In this study, we focus on the first approach.

H-adaptivity can rely either on element splitting [18, 19, 20], which requires handling non-conforming elements and hanging nodes, or on metric-based remeshing [21, 22, 23, 24]. The first approach can be used for partial remeshing of regions of interest while leaving the rest of the mesh untouched, and is thus cheaper, but less flexible since it strongly depends on the initial mesh structure and only partial anisotropic behavior can be extracted. The second one is much more flexible and well suited for the refinement of highly anisotropic flow patterns, such as shocks, boundary layers, or geometrical singularities (corners or sharp edges). However, it is also more costly, because of the recurrent calls to a mesh generator and successive interpolations.

Of particular interest here is the element splitting with hanging nodes technique, where the resulting meshes are characterized by nodes on edges and faces that are not vertices of all the cells sharing those edges or faces. When refining a mesh with this approach, every initial "parent cell", selected for refinement by a given marking criterion, is divided into "children cells". The element splitting can be isotropic or anisotropic. Element splitting-based mesh adaptation is mainly performed on (initially) structured hexahedral meshes, however, some examples of non-conformal element splitting based on triangular/tetrahedral meshes can be also found in the literature [25]. In isotropic refinement, cells are split along all the principal directions [26, 27], while in anisotropic refinement, the division is applied only along some dominant direction(s) [28].

Most of the above-mentioned studies focused on the solution of the inviscid (Euler) flow equations [29, 30] or of the Reynolds Averaged Navier–Stokes equations [31, 21]. However, the increasing demand for higher fidelity simulations such as LES or HRLES, has recently fostered efforts toward mesh adaptation strategies for scale-resolving turbulent flow simulations. In the following of this study, we focus on h-type isotropic mesh adaptation and on adaptation criteria suitable for HRLES. Mesh adaptation criteria are generally based on the estimation of the discretization error. The latter depends on the characteristic size h of the mesh used to discretize the physical domain and on the order of accuracy p of the numerical scheme used to approximate the governing equations on the given mesh. Moreover, for turbulent flows, modeling errors are also introduced, which may be coupled with discretization errors. This is particularly critical for LES approaches (and, consequently, also for HRLES). LES relies on the solution of the filtered Navier–Stokes equations, where the filter size is supposed to be known and related to the mesh size. However, due to numerical approximation errors, the actual filter size is also strongly dependant on the transfer function of the

discretization scheme. Very often, the implicit filtering error, although recognized as an additional source of error in LES, is neglected. In the literature, an attempt to quantify modeling and discretization errors in turbulent flow simulations has been proposed in [32], with particular attention to LES models, stressing the difficulty of segregating the two sources of error without using several grids of varying density. A thorough discussion on LES requirements can be also found in [33] and references cited therein. Mesh adaptation for LES, and consequently HRLES, changes the filter size both directly –through mesh resolution–, and implicitly –through the associated numerical scheme transfer function. Based on the observation that one way or another, the grid size scales with the filter width, Toosi *et. al.* proposed in [18] an anisotropic error estimator for LES problems by looking at the energy in a directional sense. The authors defined a directional error estimator based on small-scale energy coupled with a modified differential filter and computed for a time-averaged field. The efficiency of this anisotropic strategy has been tested on statistically stationary applications and stationary grids. As the authors state, this refinement criterion is not suitable for problems where strong physical features, such as shocks, interact with the turbulent field. Pope [34] suggested that a measure of the proportion of modeled to resolved kinetic energy is sufficient to assess the local accuracy of an LES computation, and showed that well-resolved LES should resolve at least 80% of the total turbulent kinetic energy. This idea has inspired several authors: for instance, Reuß *et al.* [35] proposed to use a sensor based on this measure where several models to compute the subgrid-scale turbulent kinetic energy are tested, and these sensors are used as indicators for local mesh refinement in the LES regions for a backward-facing step problem. Nevertheless, the authors also showed the efficiency of the sensor is problem and SGS model dependent. A combination of mesh refinement criteria to deal with the discretization error while ensuring enough explicit resolution of turbulent scales has been proposed in [36]. An estimate of the interpolation error of the time-averaged velocity field through the second order derivative is proposed to deal with the discretization error in all the computational domain, whereas the proportion of the total turbulent kinetic energy explicitly solved, is used as a second refinement criterion as suggested in [34]. Although this approach is promising, it remains costly and limited by the remeshing library performance, which does not allow for surface refinement.

This short state-of-the-art on mesh refinement methods for HRLES problems further motivates us to investigate the performance of a dynamic mesh adaptation framework suitable for industrial applications where new challenges are formulated, such as: (i) what could be a suitable mesh

refinement criterion that would be applicable to a variety of problems of industrial interest, and (ii) how to deal with the unsteadiness of the problems of interest while maintaining a reasonable computational cost.

In this paper we address these issues and propose a novel dynamic mesh refinement procedure where the mesh refinement criterion is directly extracted from a k-exact finite-volume scheme correction terms. The dynamic AMR procedure is completed with a combined strategy where the refinement criterion is averaged on the time interval of adaptation and a dynamic strategy is used to adaptively define the mesh adaptation period (time interval).

The paper is structured as follows: first, the methodology used to solve our problems of interest is presented in Section 2, including the k-exact numerical scheme used to solve the compressible state system of equations. In Section 3 we introduce the grid refinement strategies including the novel error criterion, the time-averaging of the adaptation criteria and the automatic period control strategy. These new implementations are tested in Numerical Results section 4 on several problems of increased difficulty, starting from a Convected Lamb Vortex where we dispose of an analytical solution suitable to validate the mesh refinement error criterion, a spatially evolving mixing layer with or without interaction with an oblique shock and lastly, a turbulent RANS/LES problem where the flow around an axisymmetric backward-facing step is considered. The paper ends with a short conclusion and perspectives.

2. Methodology

2.1. Governing equations

We look for numerical solutions of the compressible Reynolds-averaged or filtered Navier-Stokes equations, supplemented by a turbulence or subgrid model, respectively. These can be formally written as a system of conservation laws of the form:

$$\frac{d}{dt}\iiint_{\Omega_{CV}} \mathbf{w}\, d\Omega + \oiint_{A_{CV}} \mathbf{F}\cdot\mathbf{n}\, dS = 0, \tag{1}$$

where Ω_{CV} is a fixed control volume with boundary A_{CV}, $\mathbf{n}$ is the outer unit normal, $\mathbf{w}$ is the conservative variable vector, and $\mathbf{F}$ is the flux density:

$$\mathbf{F} = \mathbf{F}_E + \mathbf{F}_V \tag{2}$$

where $\mathbf{F}_E$ is the inviscid flux and $\mathbf{F}_V$ is the viscous flux.

In RANS/ LES regions of the computational domain, **w** represents the averaged/filtered flow quantities, respectively. From a more general viewpoint, **w** represents the resolved part of the flow, i.e, the larger scales of motion captured by the calculation, which eventually reduce to the mere average field for full RANS. RANS/LES are performed by using an eddy viscosity model. The eddy viscosity ν_t is determined by means of the Delayed Detached Eddy Simulation model (DDES) of [2]. In addition, the present implementation of the DDES model is based on a compressible version $k-\omega$ SST two-equation model. Wall functions are applied near solid boundaries to allow grids with a typical size of the first cell close to the wall (in wall units) of approximately 50 viscous units.

2.2. K-exact Finite Volume scheme

System (1) is approximated by means of a finite volume methodology on unstructured grids. The computational domain Ω_{CV} is partitioned in N finite volume cells Ω_J with boundary A_J, such that:

$$\Omega_{CV} = \bigcup_{J=1}^{N} \Omega_J \quad \text{and} \quad A_J = \bigcup_{K=1}^{P} A_{JK} \tag{3}$$

where index K denotes the k^{th} neighbor, Ω_K, to cell Ω_J and A_{JK} the interface between two neighbors:

$$A_{JK} = \Omega_J \cap \Omega_K \tag{4}$$

In the present finite-volume approach, the problem unknowns are represented by the cell-averaged conservative variables. The system of conservation laws referred to a computational cell then writes:

$$|\Omega_J| \frac{d\overline{\mathbf{w}}_J}{dt} + \sum_{K=1}^{P} \iint_{A_{JK}} \mathbf{F} \cdot \mathbf{n} \, dS = 0 \tag{5}$$

where $|\Omega_J|$ denotes the cell volume, the overbar denotes the cell average, and P is the number of faces of cell Ω_J.

The fluxes in equation (5) are approximated by means of a k-exact finite volume scheme of third-order accuracy (or 2-exact) proposed by Pont *et al.* in [1], following the ideas initially developed by [37].

The latter relies on the recursive correction of the approximation errors of the solution and its successive derivatives, starting with a low-order (first order, or 0-exact) approximation. Hereafter, we first briefly recall the main steps used for the k-exact reconstruction procedure. The flux function **F** is expanded in Taylor series around an integration point Γ of A_{JK}:

$$\iint_{A_{JK}} \mathbf{F} \cdot \mathbf{n} \, dS = \mathbf{F}|_\Gamma \cdot \mathcal{S}^{(0)}_{A_{JK}} + \mathbf{D}^{(1)} \, \mathbf{F}|_\Gamma \cdot \mathcal{S}^{(1)}_{A_{JK}} + \frac{1}{2}\mathbf{D}^{(2)} \, \mathbf{F}|_\Gamma \cdot \mathcal{S}^{(2)}_{A_{JK}} + |A_{JK}| O(h^n) \tag{6}$$

where $\mathbf{D}^{(l)}\,\mathbf{F}|_\Gamma$ is the l^{th} tensor derivative of $\mathbf{F}$ at point Γ, $\mathcal{S}^{(m)}_{A_{JK}}$ represents the m^{th}-order moment of A_{JK}, and h is a characteristic grid size. Specifically, $\mathbf{D}^{(1)}\mathbf{F}\big|_\Gamma$ is the flux gradient at point Γ and $\mathbf{D}^{(2)}\mathbf{F}\big|_\Gamma$ is the Hessian. Furthermore,

$$\mathcal{S}^{(0)}_{A_{JK}} = \frac{1}{|A_{JK}|}\iint_{A_{JK}} \mathbf{n}\,dS, \quad \mathcal{S}^{(1)}_{A_{JK}} = \frac{1}{|A_{JK}|}\iint_{A_{JK}} (\mathbf{x}-\mathbf{x}_\Gamma)\mathbf{n}\,dS, \quad \mathcal{S}^{(2)}_{A_{JK}} = \frac{1}{|A_{JK}|}\iint_{A_{JK}} (\mathbf{x}-\mathbf{x}_\Gamma)\otimes(\mathbf{x}-\mathbf{x}_\Gamma)\mathbf{n}\,dS \tag{7}$$

are the m^{th} order surface moments of face A_{JK}. For further convenience, we also introduce the m^{th} order volume moments $\mathcal{M}^{(m)}_J$ of Ω_J, defined as :

$$\mathcal{M}^{(m)}_J = \frac{1}{|\Omega_J|}\iiint_{\Omega_J} (\mathbf{x}-\mathbf{x}_j)^{\otimes m} d\Omega \tag{8}$$

In the preceding definitions we use the shortcut notation:

$$\mathbf{v}^{\otimes m} = \overbrace{\mathbf{v}\otimes\mathbf{v}\otimes ...\mathbf{v}}^{m \quad \text{times}}, \quad \mathbf{v}^{\otimes 0} = 1, \quad \mathbf{v}^{\otimes 1} = \mathbf{v} \tag{9}$$

with $\mathbf{v}$ a generic vector and with $\otimes$ the dyadic product. As a consequence, $\mathbf{v}^{\otimes m}$ is an mth-order tensor, and so are $\mathcal{S}^{(m)}_{A_{JK}}$ and $\mathcal{M}^{(m)}_J$.

To achieve a n^{th}-order approximation of the surface integral, the flux and its derivatives at point Γ must be reconstructed from cell-centered averages $\overline{\mathbf{w}}_J$. For robustness reasons, the reconstruction is applied to the primitive variables:

$$\mathbf{q} = (u, P, T)^T \quad \text{with} \quad \mathbf{q} = \mathbf{q}(\mathbf{w}) \tag{10}$$

Precisely, for a perfect gas with constant isentropic exponent γ, the primitive and conservative variables are linked by the following relations:

$$u = \frac{(\rho u)}{\rho}, \qquad P = (\gamma-1)\left((\rho E) - \frac{1}{2}\frac{|\rho u|^2}{\rho}\right), \qquad T = \frac{P}{\rho R} \tag{11}$$

We introduce for each cell J the vector $\widetilde{\mathbf{q}}_J = \widetilde{\mathbf{q}}(\overline{\mathbf{w}}_J)$ obtained by applying the relations (11) to the cell-averaged conservative variables $\overline{\mathbf{w}}_J$:

$$\widetilde{q}_J = (\widetilde{\mathbf{u}}_J, \widetilde{P}_J, \widetilde{T}_J)^T \tag{12}$$

The quantities $\widetilde{q}_J$ are only second-order approximations of the pointwise values of the primitive variables at the cell center $\mathbf{x}_j$. A third-order approximation is then obtained by reconstructing the primitive variables in each cell by Taylor-series expansion truncated to second-order terms:

$$\mathbf{q}(\mathbf{x}) = \mathbf{q}_j + \mathbf{D}^{(1)}\mathbf{q}\big|_j \cdot (\mathbf{x}-\mathbf{x}_j) + \frac{1}{2}\,\mathbf{D}^{(2)}\mathbf{q}\big|_j \cdot (\mathbf{x}-\mathbf{x}_j)\otimes(\mathbf{x}-\mathbf{x}_j) + O(h^3) \tag{13}$$

and by approximating $\mathbf{q}_j$, $\mathbf{D}^{(1)}\mathbf{q}\big|_j$, and $\mathbf{D}^{(2)}\mathbf{q}\big|_j$ at order 3, 2, and 1, respectively. Equation (13) represents then an approximate deconvolution operator of third-order accuracy for the primitive variables. Expanding the primitive variable $\mathbf{q}$ around the cell center $\mathbf{x}_j$, and by averaging over the cell Ω_J, gives:

$$\mathbf{q}_j = \overline{\mathbf{q}}_J - \frac{1}{2}\mathcal{M}_J^{(2)} : \mathbf{D}^{(2)}\mathbf{q}|_J + O(h^3) \tag{14}$$

Taylor expansions are also used to determine a high-order approximation of the cell-averaged primitive variables

$$\overline{\mathbf{q}}_J = \widetilde{\mathbf{q}}_J + \Delta\mathbf{q}\big|_J + O(h^n) \tag{15}$$

The correction term $\Delta\mathbf{q}\big|_J = (\Delta\mathbf{u}|_J\,, \Delta P|_J\,, \Delta T|_J)^T$ depends on the primitive variable under consideration. For instance, the correction term for the velocity field is:

$$\Delta\mathbf{u}|_J = \overline{\mathbf{u}}_J - \widetilde{\mathbf{u}}_J = \frac{1}{\overline{\rho}_J}\mathcal{M}_J^{(2)} : \left(\mathbf{D}^{(1)}\rho\big|_j \otimes \mathbf{D}^{(1)}\mathbf{u}\big|_j\right) + O(h^3) \tag{16}$$

where, for a perfect gas, the density gradient is expressed in terms of pointwise primitive variables as:

$$\mathbf{D}^{(1)}\rho\big|_j = \frac{\mathbf{D}^{(1)}P\big|_j \otimes \mathbf{D}^{(1)}T\big|_j}{RT_j} \tag{17}$$

which requires a 1^{st}-order approximation of the primitive variable gradients at point $\mathbf{x}_j$ to achieve a third-order approximation for $\Delta\mathbf{q}\big|_J$. The full expressions including formulation of the correction term for the temperature can be found in [1]. In the same reference, it was shown that including the deconvolution term in the solution reconstruction is of crucial importance to achieve truly third-order accuracy even for weakly compressible flow cases, such as the inviscid advection of a vortex: when such a term is neglected, the solution convergence order decays to a value in between second and third-order only.

Finally, combining Eqs (14) and (15), a high-order approximate deconvolution is obtained, allowing to compute the pointwise primitive variables:

$$\mathbf{q}_j = \widetilde{\mathbf{q}}_J + \Delta\mathbf{q}\big|_J - \frac{1}{2!}\mathcal{M}_J^{(2)} : \mathbf{D}^{(2)}\mathbf{q}|_J + O(h^3). \tag{18}$$

Of note, for all variables the $\Delta\mathbf{q}\big|_J$ term accounts for velocity and density variations, while the third term in Equation (18) is related to the Hessian of the corresponding field, weighted by the second-order volume moments of cell J.

To complete the procedure, high-order approximation of the gradients are obtained by following the successive correction procedure described in [1], to which the reader is referred for details. The

polynomial reconstruction formula (13) is finally used to evaluate left and right states on both sides of cell faces A_{JK}, and an exact 1D Rieman solver in the face-normal direction is used to obtain the final estimate of the numerical flux $\mathbf{F}_\Gamma$. Limiters are applied to the reconstructed left and right primitive variables in order to enforce monotonicity constraints [38].

2.3. Error estimator

The approximate deconvolution formula (18) measures the error committed by approximating the values of the primitive variables at a cell center with direct computations from the problem unknowns, i.e. the cell-averaged conservative variables. More precisely, the correction terms on the right-hand side are an estimate of the truncation error in the local solution expansion for the 1-exact scheme. Theoretically, since we are using a 2-exact scheme, an estimate of the higher-order error would be needed. However, this would require information about the third-order derivatives of the solution fields, which is difficult to obtain on general unstructured meshes, and also represents a significant overhead in both computational time and memory. To avoid this, we argue that since the k-exact scheme uses successive corrections of the truncation error to reach third-order accuracy, the truncation error of the uncorrected scheme (1-exact scheme) is a good low-cost proxy for the error of the corrected one (2-exact). This strategy is inspired by approaches commonly used for finite-element schemes (see e.g. [15]) where the decay of spectral coefficients from one order of reconstruction to the next is used as an estimate of the local interpolation error. In short, we assume that the regions where the 1-exact and 2-exact reconstructions differ the most are also those that require refinement, while the two reconstructions show little difference in regions where the solution varies slowly or in very small cells. In fact, both correction terms on the right-hand side tend to zero in the vanishing mesh size limit.

For this reason, we advocate the use of the corrective terms in (18) as indicators for local solution accuracy. More precisely, given any primitive variable q, we introduce the following error estimator, referred-to in the following as TEC_q (Truncation Error Criterion), where the subscript q stands for the primitive variable it is based on (e.g. TEC_p denotes a criterion based on the error term for the pressure):

$$TEC_q = |\Delta Q_1| + |\Delta Q_2| \tag{19}$$

with

$$\Delta Q_1 = \Delta q \tag{20}$$

and

$$\Delta Q_2 = \frac{1}{2}\mathcal{M}_J^{(2)} : \mathbf{D}^{(2)}q|_J \tag{21}$$

We employ the sum of absolute values to provide a majoration of the error, which corresponds to a more conservative estimate than the original error term. Such an approach is often preferred in the literature when estimating errors as sum of multiple terms (see for instance Refs [15],[18],[29]). Of note, while the ΔQ_1 term only requires approximations of the solution gradients, which are available for both a 1-exact (2nd-order) and 2-exact (3rd-order) scheme (although $\mathbf{D}^{(1)}q|_J$ is approximated at 1st-order for a 1-exact scheme and at 2nd-order for a 2-exact scheme), the ΔQ_2 term requires an approximation of $\mathbf{D}^{(2)}q|_J$, which is only available for a 2-exact scheme. Thus, the evaluation of ΔQ_2 represents an extra cost when using a 1-exact scheme, while it is made directly available by the third-order successive correction procedure. In the calculations, the raw error estimator (19) is normalized by using the maximum and minimum value in the flow field, so that the normalized estimators always takes values between 0 and 1.

3. Grid refinement strategy

The proposed scheme and error estimator are implemented in , the unstructured finite-volume solver developed by ArianeGroup to calculate compressible, multidimensional, unsteady, viscous and reactive flow over bodies in relative motion. FLUSEPA relies on a conservative overset grid technique initially developed to address the issues of multiple bodies in relative motion [39, 38]. The latter uses geometric intersections of a hierarchy of grid patches each assigned with a priority level to generate a single unstructured mesh: the higher priority level grids cut the lower priority ones (see Figure 1). The mesh faces resulting from the exact geometric intersection between grid cells are then used to compute the numerical fluxes as described in Section 2.2, so that the numerical discretization is intrinsically conservative.

The code also uses a dynamic mesh adaptation strategy based on isotropic octree-splitting. A high-order projection technique is used to distribute the solution from a parent cell to children cells without spuriously producing new extrema [40, 41]. The existence of octrees is invisible to the solver, which is face-based and treats cells as general polyhedra. Thus, there are no hanging nodes and no ghost cells to treat faces between two levels of refinement. Various refinement criteria, both geometric or feature-based are available in the code. The latter can be combined to generate composite criteria. Geometric criteria include the Hessian of various fields (e.g. the velocity Hessian), the pressure gradient, and the Ducros criterion [42]. More details can be found

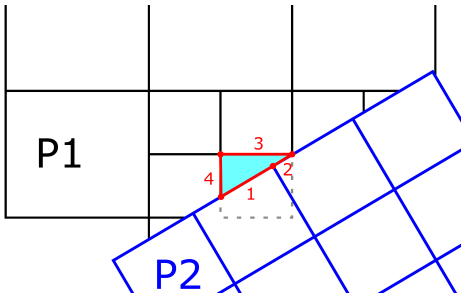

Figure 1: Illustration of the meshes overlap for two priority meshes P2 and P1, with P2>P1. Visual of the novel faces obtained after intersection.

in [43]. The mesh cells can be refined or coarsened, according to two user-defined thresholds. The adaptation criterion defined in Eq. (19) is also implemented FLUSEPA. In the numerical tests, we compare such criterion to selected heuristic and geometric criteria available in FLUSEPA. We also investigate the effect of using the two contributing terms $|\Delta Q_1|$ and $|\Delta Q_2|$ altogether or separately.

3.1. Time-averaged criteria

Dynamic mesh adaptation comes at the overcost of recomputing the metrics of the adapted mesh cells at each adaptation iteration. In addition, the solution must be projected from parent to children cells, potentially introducing interpolation errors. Most importantly, in scale resolving simulations of turbulent flows (LES or HRLES), the local grid size is directly related to sub-grid scale filtering and to the allocation of RANS and LES regions, which perturbs turbulence development and, in case of abrupt mesh refinement, may lead to catastrophic commutation errors [44, 45, 46] or to grid-induced separation in HRLES [2]. For all these many reasons, mesh adaptation is not performed at each time step of an unsteady flow computation, but at pre-defined time intervals, as sketched in Figure 2. If DMA is performed using the instantaneous error criterion computed at time T_n, the same adapted mesh is then be used to compute the solution until the next adaptation time T_{n+1}, which might lead to a loss of information if the adaptation interval is too long compared to the characteristic time scales of interest. This problem is known as the mesh/solution delay. On the contrary, if the time adaptation interval is too short compared to the flow time scales, the adaptation is accomplished too frequently, introducing an unnecessary computational overload.

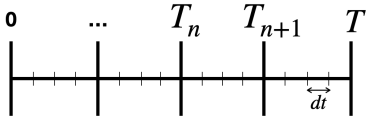

Figure 2: Illustration of time interval splitting using time slots T_n.

A possible solution, especially in configurations for which the spatial resolution requirements do not vary significantly over time (statistically steady or periodic turbulent flows), consists in averaging the refinement criterion over several time steps. An averaging strategy of the refinement criterion was recently used by Mozaffari *et al.* [47] to avoid over-refinement in HRLES simulations.

The choice of the averaging and adaptation intervals remains however open to discussion. In the present work, both intervals are chosen to be equal. The adaptation interval is selected empirically based on the flow time scales that are expected to be relevant. This is equivalent to using a phase averaged error criterion related to the characteristic time of the large flow scales, i.e. the scales of importance in hybrid RANS/LES simulations. The effectiveness of this choice is illustrated by numerical experiments in Section 4.

Using a mean criterion allows to account for time-evolution of the refinement criterion, improving the mesh delay with regard to the solution evolution. This solution however is proposed at fixed adaptation intervals and does not account directly for the dynamics of the solution. In the next subsection we propose a simple adaptive strategy, named Automatic Period Control (APC), that accounts for the refinement criteria behavior in between two consecutive mesh adaptations to either reduce the initial refinement interval or increase it. Both of these mesh refinement improvements for unsteady problems are validated and tested in Section 4.

3.2. Automatic Period Control (APC)

As mentioned before, DMA is generally performed at regular time intervals specified by the user. When little or none is known about the flow, properly selecting the adaptation period may be a challenging and time consuming task, which may require some trial and error. Choosing a mesh-adaptation time period is in itself an optimization problem, since ideally one should adapt the mesh when the flow evolves to such an extent that the current mesh is no longer capable of accurately capturing these changes. In this paper, we introduce a simple strategy (Adaptive Period Control, APC) for the adaptive and dynamic selection of the adaptation period, based on the variation of the mean error criterion between two successive mesh adaptations. More precisely, we compute a

scalar quantity ϵ that is defined as :

$$\epsilon = \frac{||\overline{c_{(n+1)}}||_{L^2(\Omega)} - ||\overline{c_{(n)}}||_{L^2(\Omega)}}{||\overline{c_{(n+1)}}||_{L^2(\Omega)} + ||\overline{c_{(n)}}||_{L^2(\Omega)}} \tag{22}$$

where $\overline{c_{(n)}}$ denotes the time-averaged adaptation criterion at time T_n, and $||\bullet||_{L^2(\Omega)}$ stands for the L^2-norm over the computational domain Ω. When the spatial norm of the adaptation criterion at time $n+1$ is much larger than the corresponding value at time n, $\epsilon \to 1$, indicating that the adaptation interval should be decreased. When $-1 \leq \epsilon \leq 0$ error variations in time are small or negative (error reduction), meaning that the physics is slow and adaptation interval can be increased. Period increase/decrease is linearly dependent on ϵ.

A typical implementation of the APC strategy is given in Algorithm 1.

Algorithm 1 Automatic Period Control (APC) algorithm.

$I \leftarrow K\Delta t$ ▷ Start with a rather small adaptation interval, $K = O(10)$
if $\epsilon \leq 0$ **then**
  $I \leftarrow I \times (1 - \epsilon)$ ▷ The adaptation interval increases because the error decreases
else if $\epsilon > 0$ **then**
  $I \leftarrow I \times (1 - \epsilon)$ ▷ The adaptation interval decreases because the error increases
end if

At the beginning of a simulation, we initialize the adaptation period as in the preceding Section, i.e. based on an estimate of the large flow time scales. If the estimate is incorrect, the averaged error estimator evolves sensibly compared to the mesh in use, and the adaptation interval is automatically reduced. The opposite is true when the flow (and then the errors) evolves slowly compared to the mesh.

4. Numerical results

In this section, we assess the mesh adaptation framework proposed in this paper by means of selected test cases of increasing difficulty. For the first inviscid test case which has an analytic solution, we aim to validate the mesh adaptation framework using the TEC_q criterion. The two following laminar problems aim to assess the efficiency of the novel mean criterion for adaptive refinement and the APC strategy to adapt the mesh refinement period. Lastly, the interest of the proposed DMA approach using mean TEC_q refinement criterion and APC is demonstrated for a

turbulent backward-facing step problem using HRLES, and specifically DDES.

The simulations are performed with the FLUSEPA solver using the finite-volume k-exact scheme summarized in Section 2.2 for the spatial resolution on unstructured hexahedra meshes and an explicit second-order time-advancing scheme (Heun scheme).

4.1. Inviscid vortex advection

Preliminary verification and validation of the proposed methodology is conducted for the well-established test case of an isentropic vortex advected by a uniform flow. The freestream Mach number is set equal to $M_\infty = 0.5$, and the flow is aligned with the horizontal axis. The vortex is superimposed as a small perturbation of the form:

$$\delta u = -U_\infty \beta \frac{(y - y_c)}{R} \exp\left(-\frac{r^2}{2}\right), \tag{23}$$

$$\delta v = U_\infty \beta \frac{(y - y_c)}{R} \exp\left(-\frac{r^2}{2}\right), \tag{24}$$

$$\delta T = \frac{(U_\infty \beta)^2}{2} \exp\left(-\frac{r^2}{2}\right), \tag{25}$$

with:

$$r = \frac{\sqrt{(x - x_c)^2 + (y - y_c)^2}}{R} \tag{26}$$

where U_∞, P_∞ and T_∞ denote the velocity, pressure and temperature of the uniform flow, R is the vortex core radius, and β is the vortex strength.

Specifically, we select the following freestream and vortex parameters:

$$P_\infty = 10^5 N/m^2, T_\infty = 300K, M_\infty = 0.5, \beta = \frac{1}{5}, R = 0.07 \tag{27}$$

The computational domain of size $[0, 4] \times [0, 2]$ is initially discretized using a uniform Cartesian grid and the vortex is advected up to time $t = 0.01$. The simulations are performed using three meshes with increasing resolution, as described in Table 1.

Meshes	MSH1	MSH2	MSH 3
Size	160×80	320×160	640×320

Table 1: Computational meshes for the convected vortex problem.

The simulations are run with a constant maximum CFL number of approximately 0.9 on all meshes. Mesh adaptation is applied every two time steps for this case, and no error estimator averaging is applied.

The influence of the initial mesh resolution and refinement levels on the mesh adaptation results are first analysed using the TEC_q criterion as a refinement indicator. We start with the coarse mesh MSH1 and apply progressively up to 2 levels of mesh refinement. The left panel of Figure 3 shows the velocity profiles at the final time, computed on the resulting adapted meshes. The more we increase the level of refinement, the more we approach the exact solution, while the initial mesh MSH1 leads to a poor representation of the velocity profile. The right panel of Figure 3 shows the influence of the initial mesh in the mesh refinement results. The three meshes MSH1, MSH2 and MSH3 are tested using different levels of refinement. We observe the results obtained using the coarse mesh MSH1 with 2 levels of refinement are as accurate as the ones obtained using MSH2 for initial mesh with one level of refinement and the fine mesh MSH3 with no refinement. The resulting curves are superimposed to within plotting accuracy. We also show in Figure 4 the velocity and pressure contours and the adapted grids starting from various initial refinement levels up to level 3. The figure shows that both adapted grid consistently apply refinement level 3 only in the region of interest, thus providing a similar accuracy to MSH3 using a smaller number of cells.

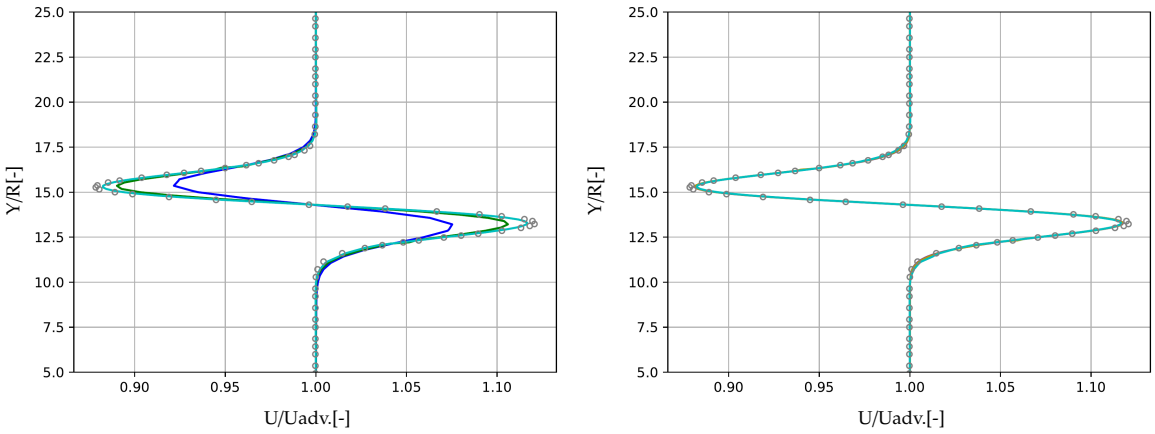

Figure 3: Left: Longitudinal velocity profiles at final time using the initial mesh MSH1 with different levels of refinement; Right: velocity profiles using various initial meshes and refinement levels: Exact Solution(○); MSH1 with no refinement (—); MSH1 with one level of refinement (—); MSH1 with two levels of refinement (—); MSH3 no refinement (—); MSH2 with one level of refinement (—)

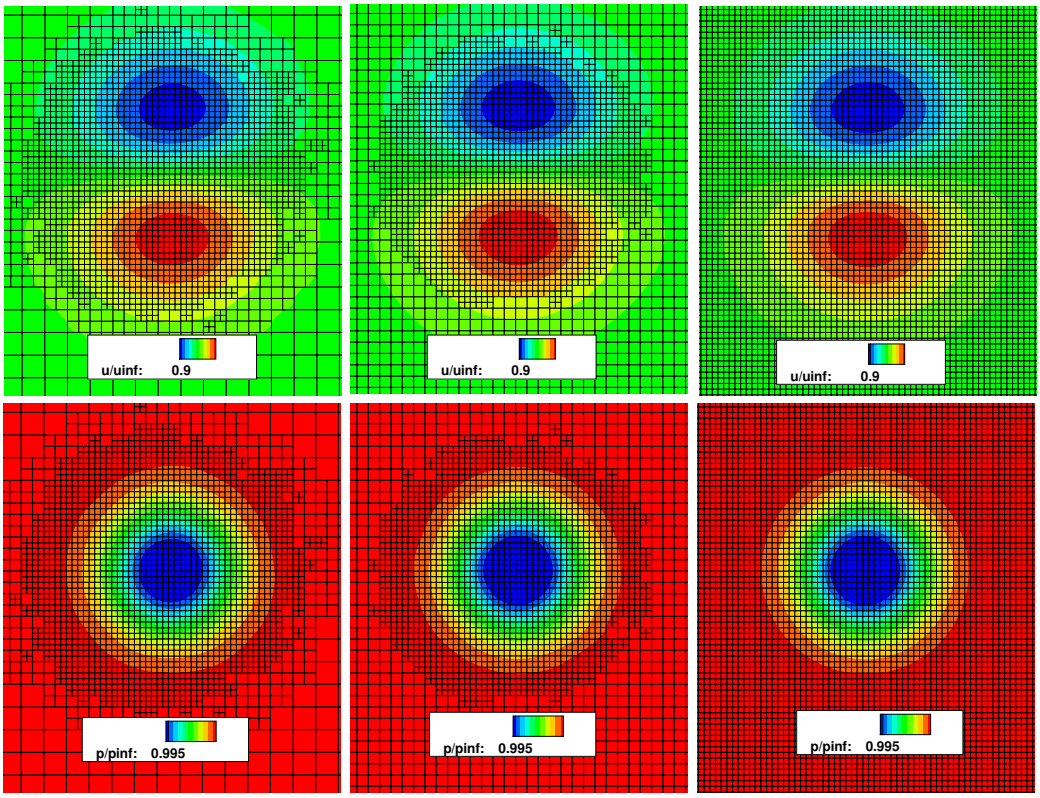

Figure 4: Top panel : u/u_{inf} : adapted mesh MSH1 with 2 levels of refinement, adapted mesh MSH2 with 1 level of refinement, uniformly adapted MSH3; Bottom panel : p/p_{inf} : adapted mesh MSH1 with 2 levels of refinement, adapted mesh MSH2 with 1 level of refinement,uniformly adapted MSH3.

Runs	$L^\infty(U)/U_{ex} \times 100$	$L^\infty(P)/P_{ex} \times 100$	Relative CPU time	Relative cell nb.
MSH1 2 refinement levels	0.4435%	0.0605%	46.0%	14.88%
MSH2 1 refinement level	0.3664%	0.0485%	61.0%	26.35%
MSH3 uniform refinement	0.3276 %	0.0462 %	100%	100%

Table 2: Longitudinal velocity L^∞ norms of the error relative to the exact solution, computational time and cell number relative to a uniformly refined grid (MSH3).

Quantitative results for the L^∞ norms of velocity and pressure errors, CPU time relative to the finest uniformly refined grid MSH3, and total number of cells are presented in Table 2. The errors are expressed as relative errors with respect to the exact solution. We observe that when using the coarse mesh MSH1 with 2 levels of refinement, the time is divided by more than two and the number of cells by 7 with respect to the uniformly refined mesh MSH3, while achieving a similar

	$L^\infty(U)$	$L^\infty(P)$	CPU time (s)	Cell number
Velocity Hessian	0.4698 %	0.0631 %	757.0	23482
Ducros	0.4009 %	0.0527 %	1812	53526
Pressure Hessian	0.4435 %	0.1228 %	1446.9	30450
TEC_P ($\|\Delta Q_1\|$)	0.4411 %	0.0605 %	714.0	21326
TEC_P $\|(\Delta Q_2\|)$	1.5437 %	0.1546 %	575.0	18862
TEC_P ($\|\Delta Q_1\| + \|\Delta Q_2\|$)	0.4252%	0.0522%	724.12	23657
TEC_U ($\|\Delta Q_1\| + \|\Delta Q_2\|$)	0.4541 %	0.0545 %	1136.2	26380

Table 3: Quantitative study: Comparison of L^∞ errors normalized with the exact solution, CPU time and cell numbers for meshes obtained using several refinement criteria.

error level. In the following, we only consider mesh refinement starting with the coarser mesh. Next, we assess the proposed mesh adaptation criterion TEC_q against other criteria available in the literature. The TEC_q criterion is computed here using either the pressure or the velocity field. The influence of each corrective term, ΔQ_1 or ΔQ_2, composing TEC_q (see Section 2.3) is also scrutinized. A quantitative analysis of the L^∞ errors, computation time and number of cells is reported in Table 3. The performance of TEC_q criterion is comparable to the considered classical heuristic criteria, a slightly better performance being obtained by using the TEC_P with both corrective terms ΔQ_1 and ΔQ_2 active.

A closer view of the results obtained using either only the first corrective term ΔQ_1, only the second corrective term ΔQ_2 or the full TEC_P criterion is given in Figure 5. The left panel shows that the velocity profile obtained on the adapted mesh refined using only ΔQ_1 in the TEC_P is already very close to the exact velocity profile, while using only ΔQ_2 in the TEC_P is insufficient for this problem. The most accurate results are obtained using both ΔQ_1 and ΔQ_2. It is also interesting to compare the accuracy of the results obtained using TEC_P computed only from ΔQ_2 with the pressure Hessian criterion since both expressions use information about the second derivative in their respective expressions. The criterion $|\Delta Q_2|$ uses a double contracted product of the Hessian with the correction matrix: on a regular cartesian grid, this implies that only the diagonal components of the Hessian (derivatives in the main directions) are taken into account. The standard Hessian criterion uses instead the Frobenius norm of the Hessian. The comparison is reported in Figure 5. In Table 3 the L^∞ error is comparatively larger than that of the other criteria. This discrepancy explains why the profiles in Figure 5 deviate more from the exact solution. We observe that the velocity profiles

obtained on the adapted mesh using the pressure Hessian are closer to the exact solution. This shows the importance of using both correction terms $|\Delta Q_1|$ and $|\Delta Q_2|$ in the definition of the TEC_q criterion.

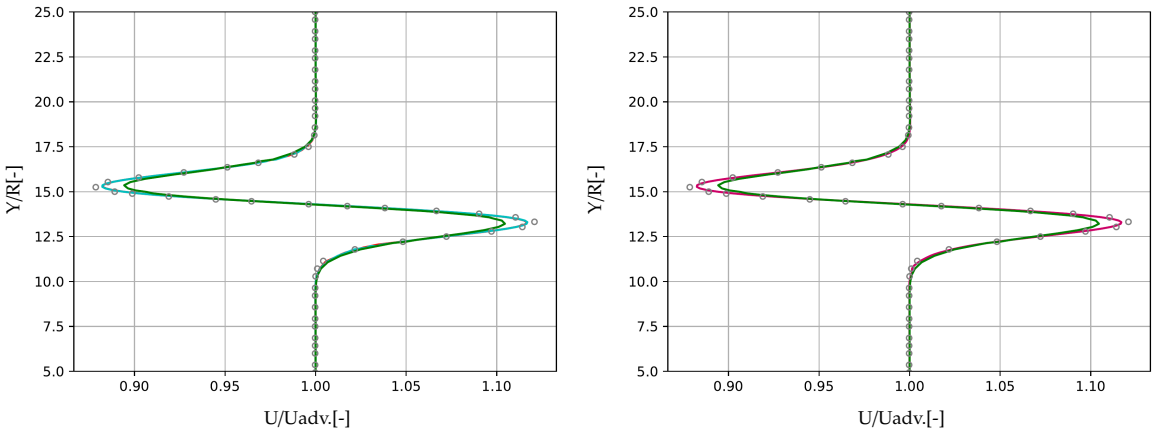

Figure 5: Left : Influence of the correction terms of the TEC_q criterion on the velocity profiles ; Right : comparison of TEC_P $|\Delta Q_2|$ term with pressure Hessian : TEC_P ($|\Delta Q_1| + |\Delta Q_2|$)(—); TEC_P ($|\Delta Q_1|$)(—); TEC_P ($|\Delta Q_2|$)(—); Pressure Hessian(—); Exact Solution(◦)

This preliminary analysis provided a first validation of the proposed dynamic mesh adaptation strategy and assessed the performance of the new mesh refinement criterion. We investigate next the effect of using the time average of the refinement criterion for unsteady problems and the coupling with the adaptive period control (APC) to account for the dynamic of the problems of interest in the mesh adaptation framework.

4.2. Spatially Evolving Mixing Layer

The effect of using the time-averaged TEC_q criterion and the APC strategy performance is assessed on a test case representative of a spatially evolving laminar mixing layer introduced in [48]. The computational domain is a rectangular box with a hyperbolic tangent velocity profile $u(x = 0, y) = 2.5 + 0.5 \tanh(2y)$ specified along the inflow boundary $x = 0$ giving a mixing layer with upper velocity $u_1 = 3$ and lower velocity $u_2 = 2$. Equal pressures and stagnation enthalpies are assumed for the lower and upper flows. The convective Mach number is $Ma_c = \frac{u_1 - u_2}{c_1 + c_2} = 0.6$ and the Reynolds number based on the initial vorticity thickness $Re = 500$. Supersonic inflow and outflow boundary conditions are imposed at the left and right boundaries, respectively. The simulations are

conducted using a constant time step corresponding to a maximum CFL number of approximately 0.8. Mesh adaptation is performed every 40 time steps, leading to an adaptation frequency of the same order of the vortex shedding frequency.

The DMA is applied next using three refinement strategies with the same initial coarse mesh. In Figure 6 we report the pressure contours obtained on the adaptive meshes at the final time $t = 4$ minutes using (a) the instantaneous TEC_q criterion as mesh refinement indicator at fixed time-adaptive period, (b) the time-averaged criterion as refinement indicator as introduced in Section 3.1 at fixed time-adaptive period and (c) the time-averaged criterion coupled with the APC technique introduced in Section 3.2 to automatically and dynamically adapt the mesh refinement period according to the physical flow evolution. In cases (b) and (c), the adaptive mesh is able to accurately capture the vortical structures. However, this is not the case for (a) where the instantaneous criterion is used, which is due to the solution-mesh delay problem. A closeup view of the adapted mesh obtained using the time-averaged criterion with APC shows that a smooth refinement is obtained, mostly concentrated in the mixing layer region as expected.

Instantaneous velocity and pressure distributions along the line $y = 0$ are presented in Figure 7. The reference values computed on a uniformly refined grid of 480×120 elements are plotted in dashed black line. We observe that the results obtained using the time-averaged criterion and APC (plain red line) are the closest to the reference solution and almost superimposed with the results obtained using the time-averaged criterion with a fixed adaptation period. Finally, quantitative results are provided in Table 4. We compare the CPU times and total mesh sizes with respect to the reference mesh. Time averaging of the refinement criterion reduces the overall number of mesh cells, and therefore the CPU time with respect to the instantaneous criterion, while reaching an accuracy comparable to the reference solution. Of note, results using the APC technique are quite close to the uniformly refined grid. As for the number of cells, it does not change much by introducing the APC, but the computational time is further reduced, because the number of adaptations decreases.

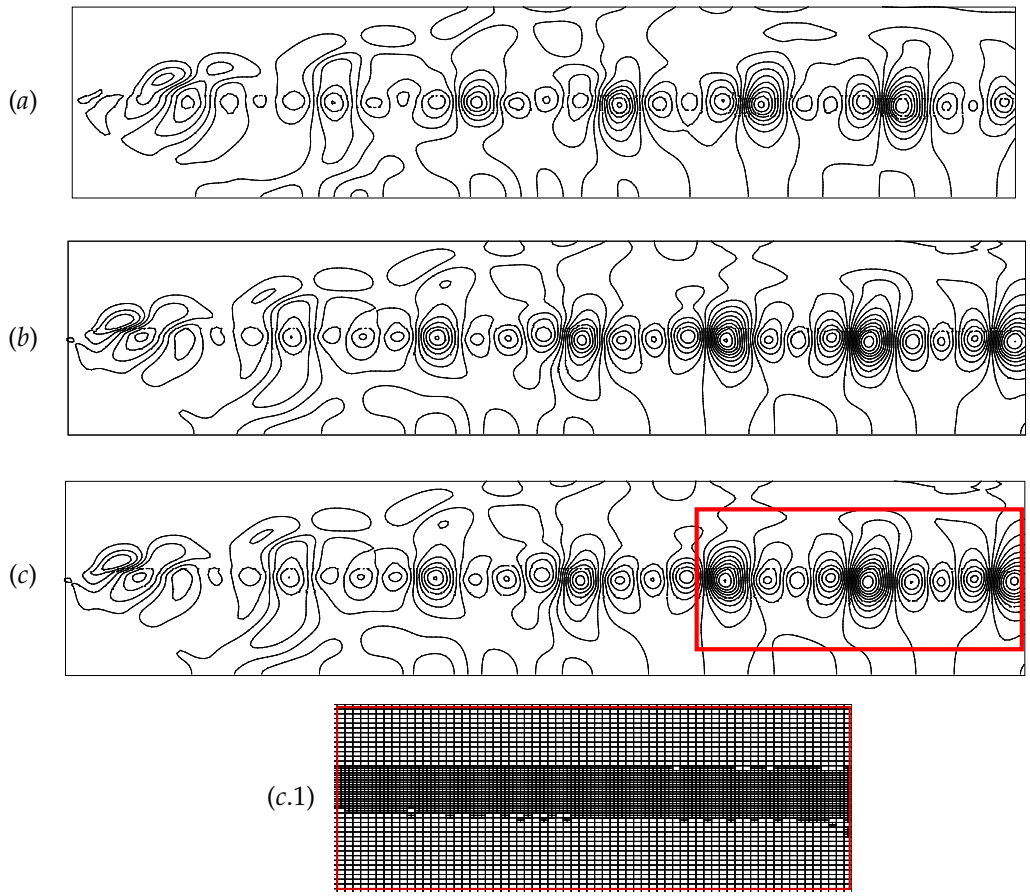

Figure 6: Mixing layer problem: pressure isocontours using a) instantaneous TEC_q criterion; b) time-averaged TEC_q criterion c) time-averaged TEC_q criterion with APC ,c.1)zoom of time-averaged criterion with APC.

To gain deeper insights into the performance of TEC_q compared to alternative criteria, a comparative analysis is conducted. The results based on the averaged TEC_q criterion with APC are contrasted with those obtained using the time averaged pressure Hessian with APC. The results are presented in Table 4 and Figure 8. It appears that, in terms of velocity and pressure profiles, the TEC_q criterion better captures the solution peaks. However, when considering computational metrics such as CPU time and cell count, both criteria demonstrate similar performance. Notably, the application of APC with both criteria, results in a reduction in both cell count and computational time.

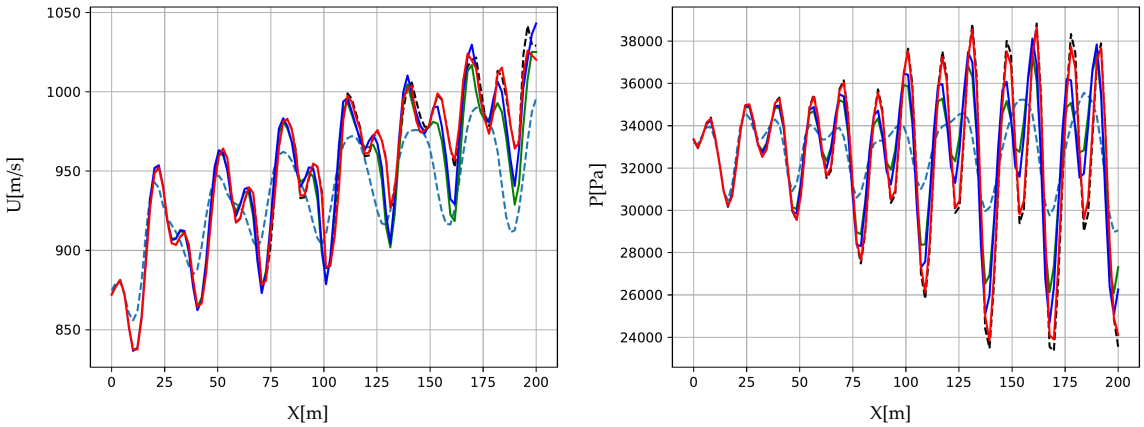

Figure 7: Comparison of velocity (left) and pressure (right) profiles along the horizontal line $y = 0$ using a uniformly refined mesh of 480×120 elements, a coarse mesh of 240×60 elements with no refinement and adaptive meshes with 1 level of refinement using TEC_q as refinement indicator with instantaneous, mean and APC techniques; 480x120 no DMA (– –); 240x60 no DMA (– –); DMA, instantaneous TEC_q criterion, (—); DMA, averaged TEC_q criterion (—); DMA, averaged TEC_q criterion with APC (—)

Mesh	Criterion	APC	Relative CPU time	Relative cell number
TEC_q	Instantaneous	no	33.47%	32.13%
TEC_q	Time-averaged	no	29.15%	29.81%
TEC_q	Time-averaged	yes	27.34%	29.85%
Pressure Hessian	Instantaneous	no	32.47%	31.18%
Pressure Hessian	Time-averaged	no	29.69%	32.66%
Pressure Hessian	Time-averaged	yes	27.46%	32.45%
Uniform 480×120.	No mesh refinement	no	100%	100%

Table 4: Computational time and mesh size comparison for adapted meshes refined using TEC_q criterion.

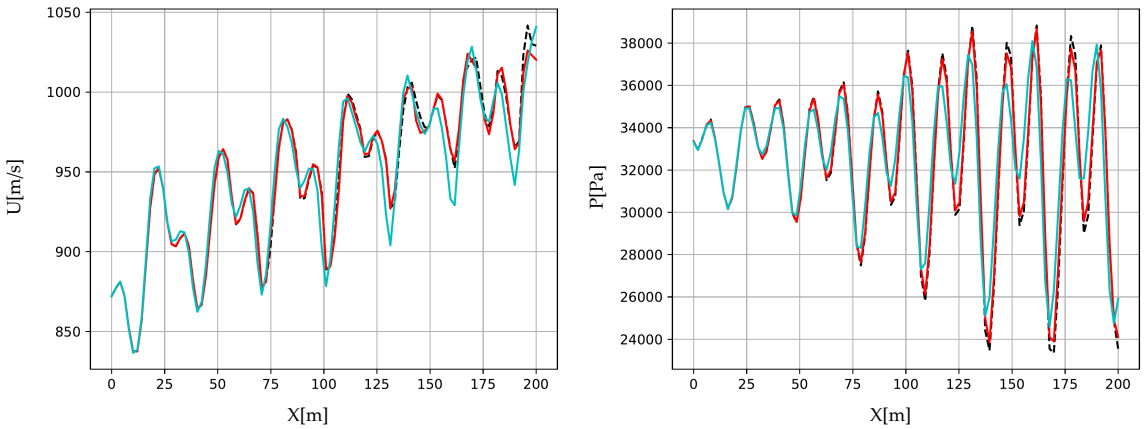

Figure 8: Comparison of velocity (left) and pressure (right) profiles along the horizontal line $y = 0$ using a uniformly refined mesh of 480×120 elements and adaptive meshes with 1 level of refinement using time-averaged TEC_q and pressure Hessian as refinement indicators along with APC; 480x120 no DMA(– –); (—); DMA, TEC_q (—)

4.3. *Shock Wave Impingement on a Spatially Evolving Mixing Layer*

In this Section, we apply the DMA framework to a flow with strong compressibility effects, namely, the interaction of an oblique shock with a supersonic mixing layer [49]. The setup is similar to the preceding test case, including the integration time step and adaptation interval. Specifically, we consider the same convective inlet velocity profile, Mach number 0.6 and Reynolds number 500. The flow state along the upper boundary is initialized such that an oblique shock is generated with an angle $\beta = 12°$ from the top left-hand corner of the domain. This shock impinges on the spatially evolving shear layer, which is deflected by the interaction. The shock wave below the shear layer reflects on the lower boundary treated as a slip wall and crosses back to the unstable shear layer. Reference results are obtained using a fine mesh of 960×240 elements. The contours of the pressure computed using the adaptive mesh with the APC technique and the time-average TEC_q criterion is displayed in Figure 9 (bottom panel). The results compare very well with the literature (top panel) and with the contours obtained on our uniformly refined reference mesh (middle panel). A closeup view of the interaction region shows that the adapted grid concentrates the cells along the shocks and in the mixing layer. It is to be noted here that the TEC_q criterion is also able to capture singularities such as shocks and their interaction without any additional shock detection technique.

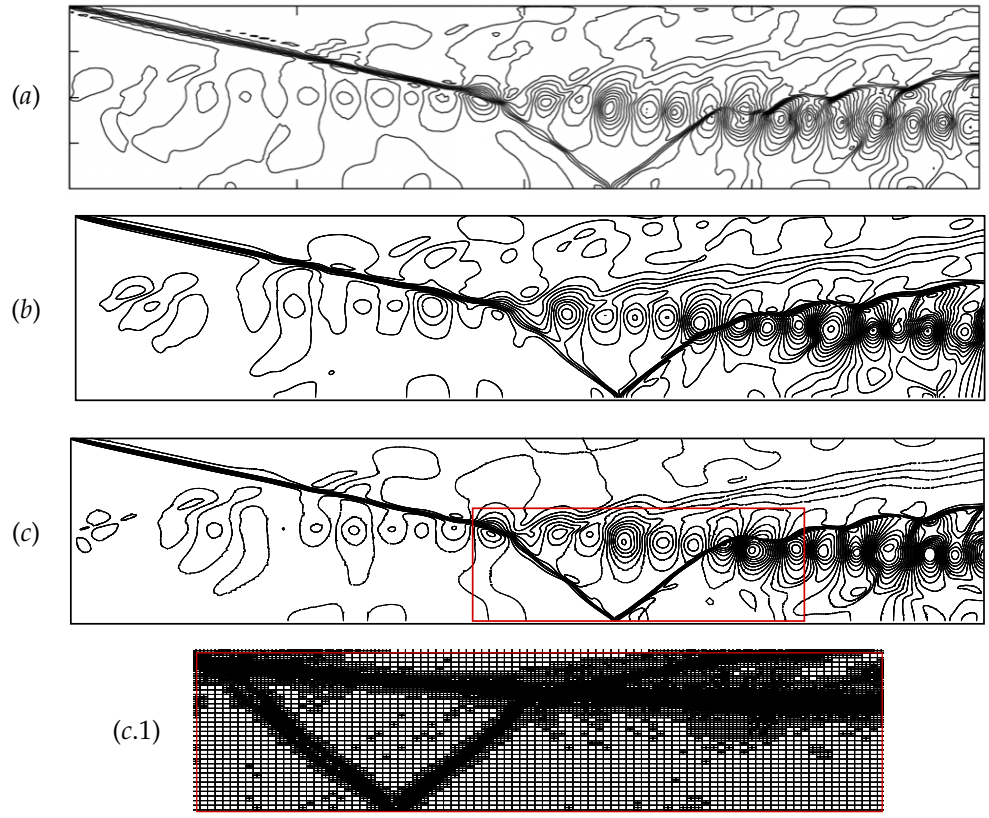

Figure 9: (a) Pressure contours extracted from [48]; (b) : Pressure contours obtained on the uniformly refined mesh of 960×240 elements; (c) Pressure contours obtained on the adaptive mesh with 2 levels of refinement using the APC technique and the time-average TEC_q refinement criterion; (c.1) zoom of the resulting adaptive mesh.

In Figure 10 the velocity and pressure profiles computed on the adapted meshes for the TEC_q and the pressure Hessian criterion are compared to those obtained on the reference mesh of 960×240 elements. The values are extracted from the cut line $y = 0$. The results obtained on the adaptive meshes show very good agreement with the reference solution with the TEC_q criterion better capturing the peaks.

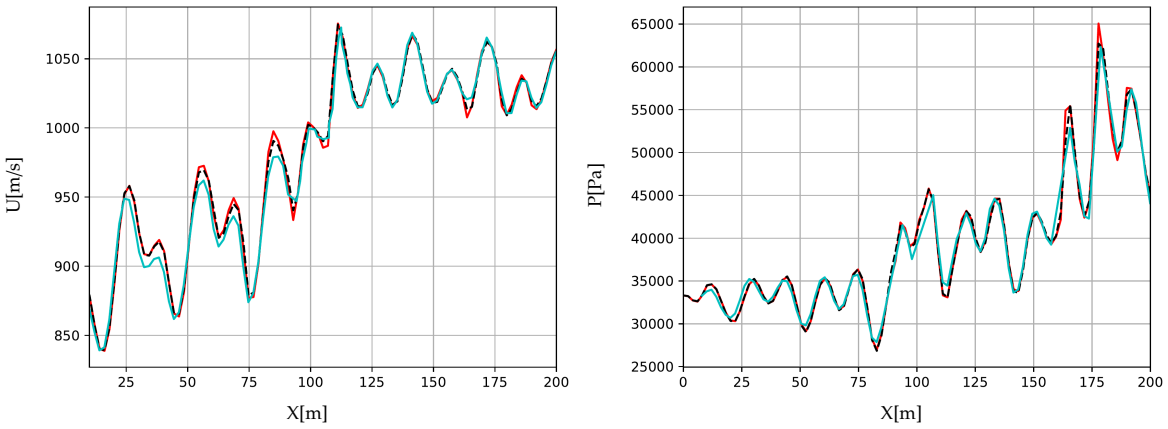

Figure 10: Comparison of velocity and pressure profiles using uniformly refined mesh of 960x240 elements (– –); and coarse mesh of 240x60 elements with 2 level of refinement using TEC_q with APC (—) and pressure Hessian with APC (—) along horizontal line $y = 0$;

4.4. *Hybrid RANS/LES of a transonic axysymmetric backward facing step*

As a final test case, we consider the transonic flow over an axysymmetric backward facing step, representative of the flow behind a space laucher. The Mach number based on free-stream conditions is equal to 0.7 and the Reynolds number based on the diameter D is set to be $Re = 1.2 \times 10^6$. The upstream length before the step is chosen so as to obtain a boundary-layer thickness of $0.2D$ just before the separation point. The length before the step is $1.8m$ and the diameter is $D = 100mm$. The geometry is shown in Figure 11(a). Numerical solutions are computed by using the hybrid RANS/LES DDES approach (see Section 2). The timestep is set to be 10^{-7}s for all simulations. The adaptation is performed every 20 time steps. This interval is small compared to the characteristic time of the large turbulent scales, but is high enough to start observing some solution/mesh delay problem if an instantaneous criterion is used. The initial mesh is made of overset intersected grids. The block containing the whole wall (represented in red in Figure 11(b)) is clustered in the boundary layer and contains about 1.5×10^6 cells. At $0.08D$ distance from the separation point, a patch grid with an initial low resolution of 3 x 10^4 cells is created (displayed in orange in Figure 11), which encompasses the whole recirculation area. The rest of the mesh is made of several background grids with lower priority levels containing a small number of cells. The maximum level of refinement in each grid is set to 3, which allows an azimuthal resolution of $Nz = 240$ cells in the recirculation area. All DMA calculations are run in parallel on 384 CPUs.

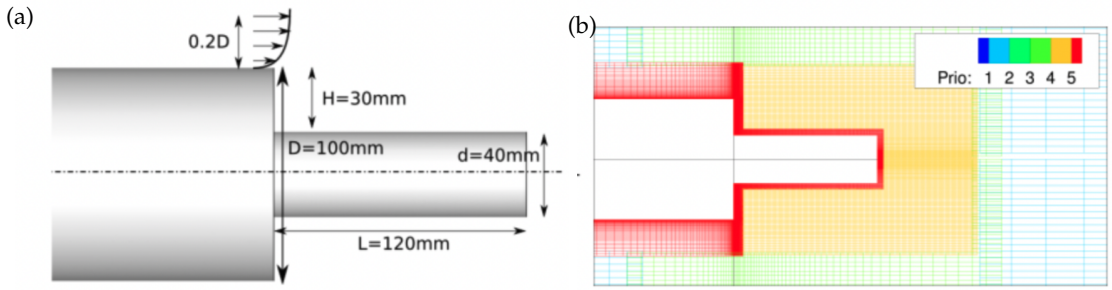

Figure 11: (a) Sketch of the cylindrical backward facing step, (b) Initial mesh, composed of overset meshes with 6 levels of priority.

We display in Figure 12 the various adapted meshes, using the instantaneous, time-averaged and APC with time-averaged TEC_q refinement criterion. The resulting meshes tend to be refined in the shear layer and around the separation point, while no refinement occurs in the attached boundary layer region where the RANS mode of DDES is active. This suggests the initial mesh is sufficiently refined to accurately capture the average flow quantities in RANS computation. We also observe that when using the time-averaged refinement criterion with a fixed adaptation period the resulting grid is more uniformly refined than with the instantaneous criterion, especially in the shear layer region, characterized by highly unsteady Kelvin-Helmoltz vortices. Using the APC further improves the refined regions and consequently the accuracy. We observe similar mesh elements distribution when using the averaged criterion with or without APC, while the instantaneous criterion leads to a more scattered and time-varying refinement, unfavourable to the development of turbulent structures.

In all cases, the near-wall region (modeled with the RANS mode of DDES) is not selected for refinement: this is a desirable property, provided that the initial grid is already sufficiently refined for RANS, since the mesh adaptation efforts can be focused on improving the resolution of turbulent scales in the LES regions. The reason is that the TEC_q criterion based on pressure derivatives takes very low values in such region. Overall, the instantaneous criterion yields approximately 11 million cells, while the mean criterion and the combined APC and mean criterion result in approximately 10 million cells each. The computational CPU time is notably lower when employing the APC technique, thanks to the dynamic adjustment of the adaptation interval. In the APC calculation, the total number of cells tends to stabilize as the solution converges toward the statistically steady state, and the refinement process is stopped once the APC criterion is satisfied.

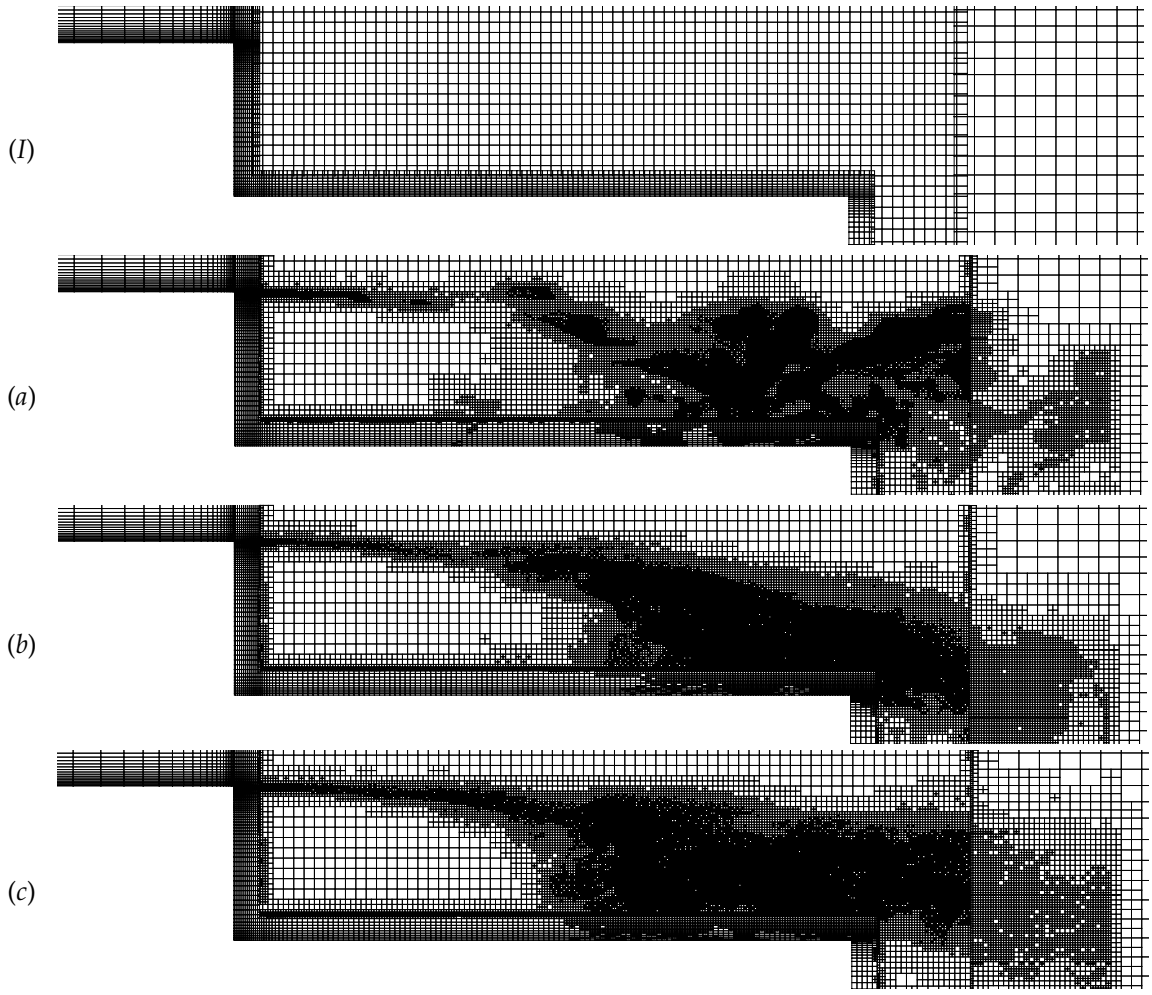

Figure 12: Initial coarse mesh (I), adapted resulting meshes using the instantaneous TEC_q refinement criterion (a), mean TEC_q criterion (b), and mean TEC_q criterion with APC (c).

Figure 13 represents a snapshot of the Q criterion, colored by the velocity magnitude, showing the coherent structures in the recirculation area downstream of the backward facing step. The figures show the development of shear layer instabilities downstream of the step, their tridimensionalization, the formation of hairpin vortices, and the breakdown to turbulence. Interestingly, the instabilities destabilize and remain axisymmetric over a longer downstream distance when using the instantaneous criterion, due to the mesh/solution delay (see Figure 13a). On the contrary, time-averaging of the criterion provides a more uniformly refined mesh in the critical shear layer region,

favouring instability development and the tridimensionalization of the flow (Figures 13b-13c).

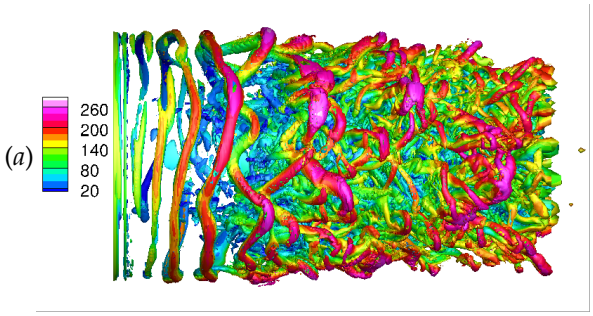

(a) Q criterion for (a) the instantaneous criterion.

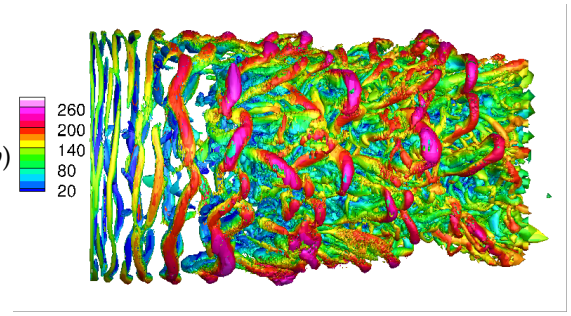

(b) Q criterion for the (b) mean criterion.

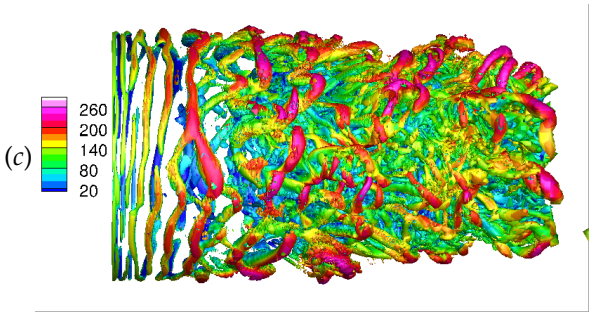

(c) Q criterion for the (c) mean criterion with the APC technique.

Figure 13: Q criterion comparisons: (a) instantaneous criterion, (b) mean criterion, and (c) mean criterion with the APC technique.

497

498 For a more quantitative assessment of the solutions, the wall distributions of the time-averaged
499 pressure coefficient and distributions and fluctuations are compared in Figure 14 with experimental
500 data [50, 51] and with the reference solution of [52], obtained on a fixed structured grid of 12×10^6
501 cells (with 240 cells in the azimuthal direction) using zonal DES for turbulence modeling. The
502 time-averaged pressure coefficient is in rather satisfactory agreement with the experimental data
503 and with the reference solution for all the adapted grids. The fluctuating pressure coefficient,
504 shown in panel (b) is also in good agreement with the experiments, when using the time averaged
505 criterion. Larger discrepancies are noticed however for the instantaneous criterion, which tends to
506 underestimate the $C_{p_{rms}}$ values.

507 Next, we analyze the time-averaged longitudinal velocity profiles and the streamwise velocity
508 fluctuations at several locations along the rear body ($\frac{x}{D} = 0.57, \frac{x}{D} = 2.3, \frac{x}{D} = 4.3$). The mean velocity
509 profiles, reported in Figure 15 are compared with the numerical results of [52]. In all cases, the

	Deprés et al. [50]	ZDES [52]	Inst.	Average	APC
X_r/D	1.13	1.15	1.12	1.12	1.12

Table 5: Experimental and numerical values of the reattachement point on the rear body.

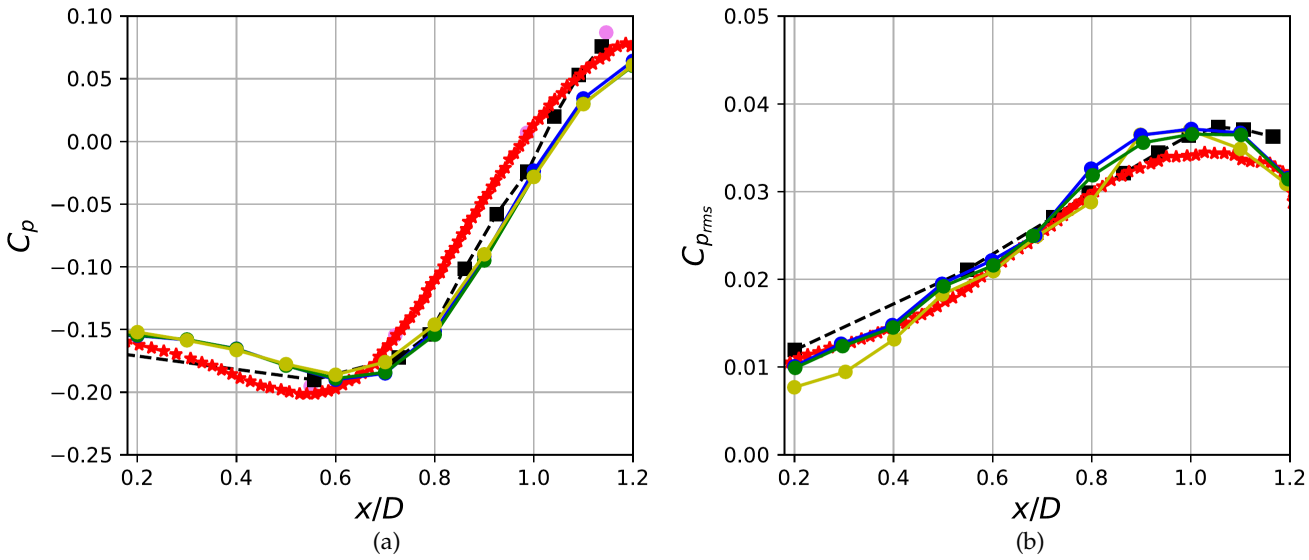

Figure 14: Pressure coefficients evolution for several adapted meshes: [52] (-★-); DMA, Time-averaged TEC_q(-●-); DMA, instantaneous - TEC_q (-●-); DMA, time-averaged TEC_q with APC(-●-); Meliga (Steady pressure taps) (●); Meliga (Kulite sensors) (-■-);

computed mean flow is characterized by a recirculation bubble, which reattaches along the rear body. The present solutions are very close to each other and to results from the literature, except for the last station. The solution obtained with the instantaneous criterion show again a somewhat larger discrepancy than the other ones. The reattachment point location along the rear body, reported in table 5, is found to be in slightly better agreement with the experimental results of [50] than the solution of [52]. We chose to compare our results with Weiss's work because he used a uniformly refined grid of approximately 12 million elements, a grid size that is comparable to what we achieved with our adapted meshes.

To further analyze the effectiveness of the proposed grid adaptation strategy for RANS/LES simulations, we estimate in the following the size of the resolved turbulent scales at two locations in the recirculation bubble, illustrated in Figure 16, where time-averaged velocity field is also

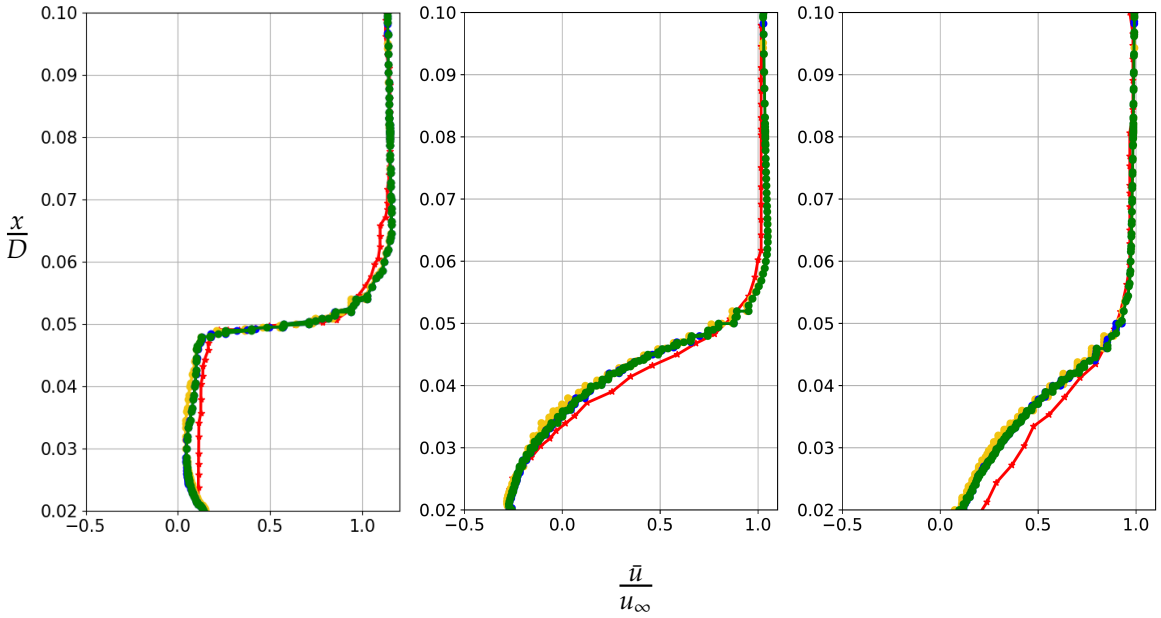

Figure 15: Time-averaged longitudinal velocity at different locations along the rear body: $\frac{x}{D}$ = 0.57 (left), $\frac{x}{D}$ = 2.3 (middle), $\frac{x}{D}$ = 4.3 (right). Results from [52] (-★-); DMA, Time-averaged TEC_q(—●—); DMA, instantaneous - TEC_q (—●—); DMA, time-averaged TEC_q with APC(—●—)

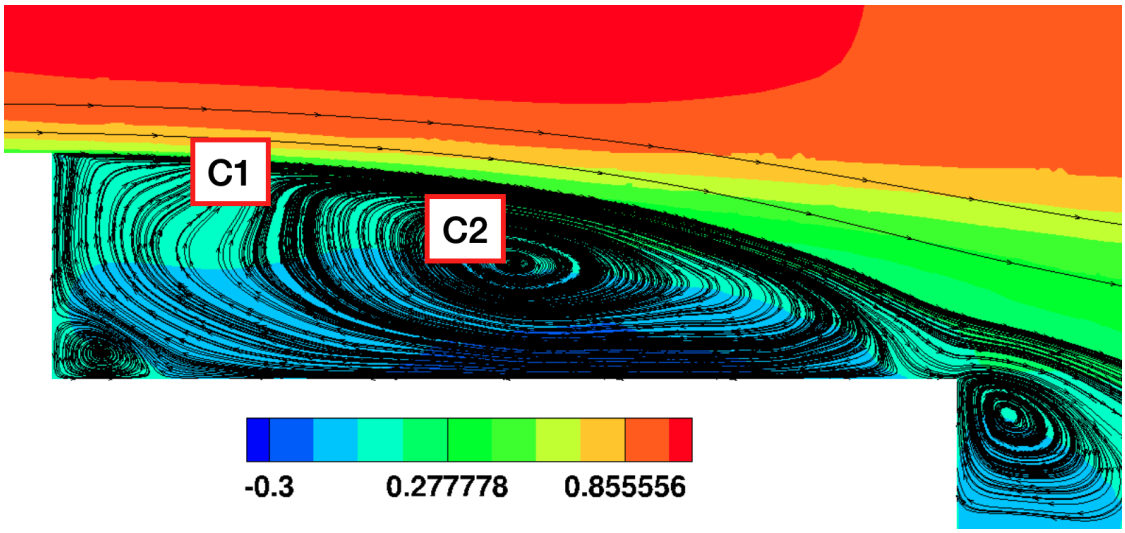

Figure 16: Mean flow velocity contours $\frac{\bar{u}}{U_\infty}$ for calculation (c) using TEC_q mean criterion coupled with APC technique, and location of points where turbulent flow scales are estimated.

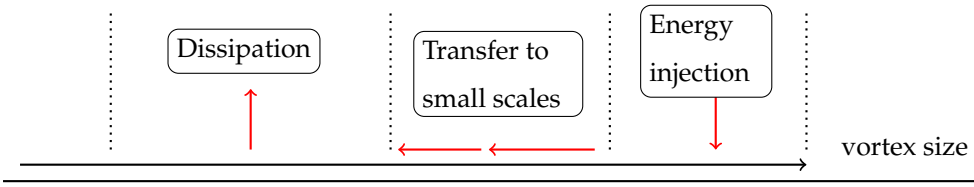

	l_η	λ	l_{DI}	H_{min}	l_{EI}	L
(a)	1.36e-6	3.52e-5	0.00055	0.0095	0.039	0.23
(b)	1.29e-6	3.46e-5	0.00056	0.0095	0.042	0.25
(c)	1.17e-6	3.2e-5	0.00052	0.0095	0.042	0.25

Table 6: Quantitative study: turbulent scales for captor 1 in Figure 16

shown. For that purpose, we make the assumption that the turbulence is locally homogeneous and isotropic, and we estimate the turbulent integral scale from $L = k^{\frac{3}{2}}/\epsilon$ with k the sum of the modeled and resolved kinetic energy and ϵ the modeled dissipation rate. Following [34], we estimate the turbulent scales marking the upper limit of the inertial range as $l_{EI} = \frac{L}{6}$. The Kolmogorov scale, related to dissipation effects, is estimated as $l_\eta = \left(\frac{\nu^3}{\epsilon}\right)^{\frac{1}{4}}$. Finally, Taylor's microscale λ is obtained as $\lambda = \left(\frac{10\nu k}{\epsilon}\right)^{\frac{1}{2}}$. We estimate such scales for the two sensors highlighted with symbols in Figure 16: sensor 1 is located in the shear layer and sensor 2 is within the recirculation bubble. The length scales are reported in Tabs. 6 and 7. The minimum grid size $H_{min} = 0.0095$m reached on the most refined grid level is significantly smaller than the estimated integral scale, but one order of magnitude larger than the estimated Taylor microscale, indicating that the simulations resolve part of the inertial range without resolving the fine-scale turbulence. In other terms, the achieved grid refinement fulfills typical RANS/LES grid resolution criteria.

Furthermore, in Figure 17 we report the ratio of the grid size to the local integral scale $\frac{h}{L}$, where h is computed as the cubic root of the local cell volume, and L is estimated from the modelled dissipation and the sum of the modelled and resolved turbulent kinetic energy. This ratio measures how fine the grid is relative to local characteristic size of the largest turbulence structures in the flow. Values between 0.005 and 0.01 are observed downstream of the step, indicating that the local grid sizes are about two orders of magnitude smaller than the integral scale, i.e. a sufficiently extended range of turbulent structures (for LES) is captured. Interestingly, simulations based on time-averaged criteria exhibit a wider region of low h/L, confirming that turbulence is better resolved in these simulations.

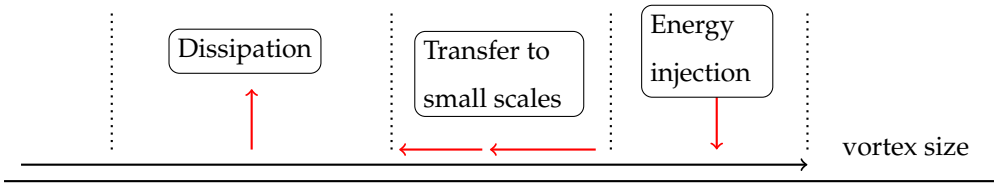

	l_η	λ	l_{DI}	H_{min}	l_{EI}	L
(a)	1.36e-6	4.24e-5	0.00046	0.0095	0.093	0.56
(b)	1.29e-6	3.87e-5	0.0005	0.0095	0.1	0.61
(c)	1.17e-6	3.14e-5	0.0005	0.0095	0.098	0.59

Table 7: Quantitative study: turbulent scales for captor 2 in Figure 16

In the RANS regions, where turbulence is modeled rather than directly resolved, the grid does not need to be as fine, and we observe that this ratio is significantly higher than in the LES regions in all cases.

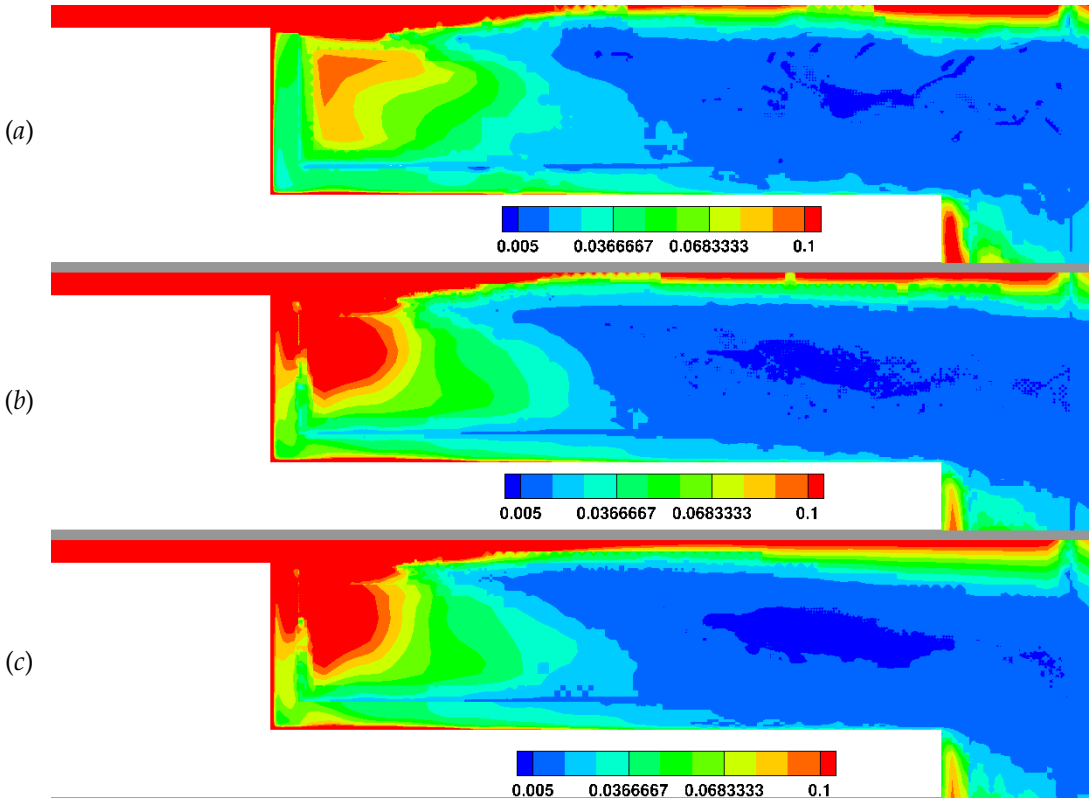

Figure 17: Ratio h/L of the local chatacteristic grid size h over the integral scale of turbulence L for (a) the instantaneous criterion, (b) the time-averaged criterion, and (c) the time-averaged criterion with the APC technique.

For additional insights, the pressure spectra are provided for specific positions at $\frac{x}{D} = 0.6$ and $\frac{x}{D} = 1.2$ for the DMA calculation using the mean TEC_q criterion coupled with the APC technique, reported in Figures 19 and 20, respectively. The spectra are computed from time signals extracted at four equally-spaced azimuthal positions, and averaged together. The objective is to capture the dominant frequencies illustrated in Figure 18 adapted from [52]. In agreement with experimental and numerical studies in the literature, the spectrum in Figure 19, exhibits a large peak centred at $St = 0.1$, while a peak is detected also at $St = 0.2$ in Figure 19. The figures also show that, at these locations, more than half a decade of the inertial range is resolved in the simulation. Finally, in Figure 20 various notable peaks ranging from $St = 0.5$ to $St = 1$ are observed, with a maximum located around $St = 0.6$, in fair agreement with other experimental and numerical results available in the literature at this location.

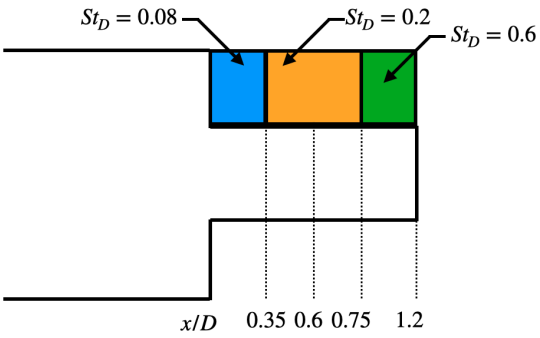

Figure 18: Spatial organization of dominating frequencies on antisymmetric backward facing step [52].

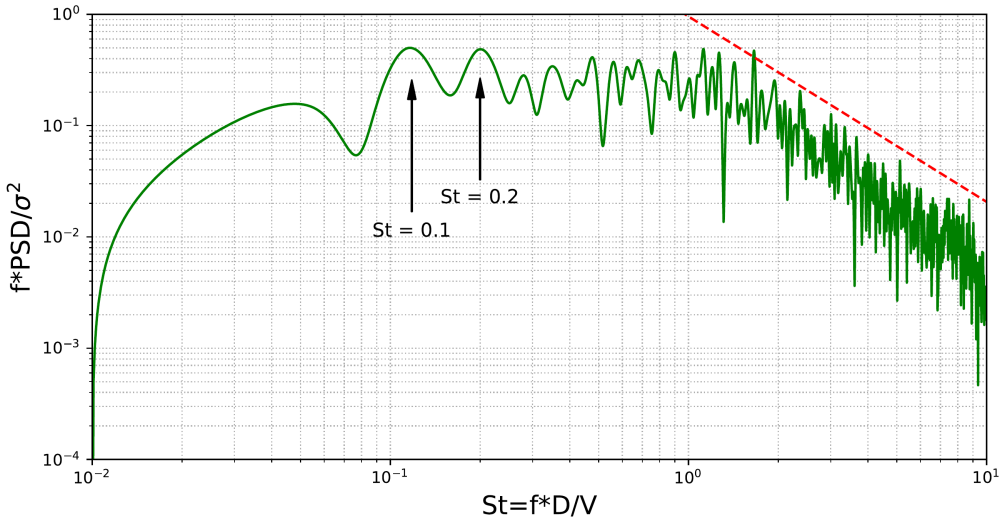

Figure 19: Normalized PSD of the pressure in log-log for the streamwise location $x/D = 0.6$ for DMA calculation using mean criterion with APC technique (c) (——) and slope at $-5/3$ (- - -) in log-log.

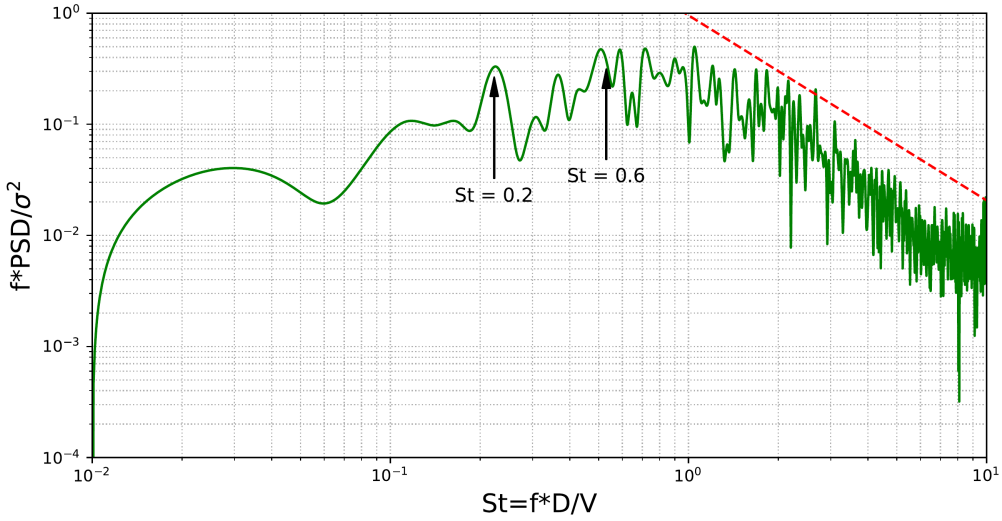

Figure 20: Normalized PSD of the pressure for the streamwise location $x/D = 1.2$ for DMA calculation using mean criterion with APC technique (c) (——) and slope at $-5/3$ (- - -) in log-log.

Figure 21 displays a linear-log axis plot of the contribution of the total energy of a frequency band thanks to the estimated power spectral density PSD function of pressure fluctuations, for the case (c) when the mean TEC_q criterion is used, coupled with the APC technique. This spectrum, located at the position $\frac{x}{D} = 0.99$, is represented with a solid green line. It is compared to the experimental data of Meliga and Reijasse [51] and Depres [50], as well as the numerical results obtained by Weiss in [52]. The dominant presence of broadband high-frequency components in the spectrum is attributed to the intensified organized shear layer structures, which progressively approach the wall before encountering it and disintegrating into smaller scales. It is also noted that that this contribution is centered around $St = 0.6$, which agrees with the observations of Mabey [53]. This is the characteristic frequency of vortical structures seen in free shear layers. In addition, this spectrum displays a peak at $St \approx 0.1$ as seen in [54]. This low frequency peak is often attributed to the "flapping" of the shear layer and reflects the overall separation-bubble growth/decay dynamics as observed in [55]. Finally, the presence of the well-known "shedding" appears through a peak near $St = 0.2$.In conclusion we observe that by using the mean TEC_q criterion with the APC technique at this particular position, we are able to capture the dominant flow frequencies, which are centered around $St = 0.6$.

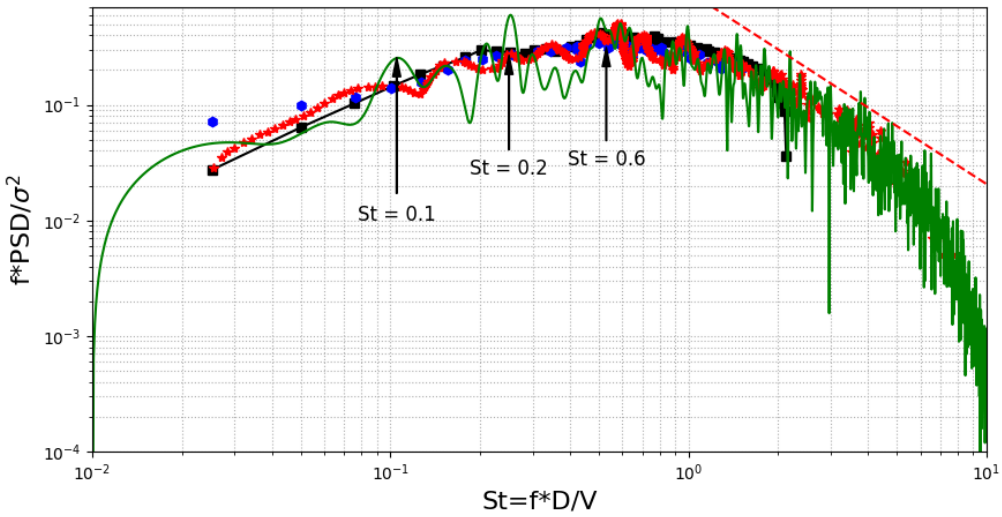

Figure 21: Comparison of normalized PSD of the pressure for the streamwise location $x/D = 0.99$ for : DMA calculation using mean criterion with APC technique (c) (——), experimental data obtained by Meliga and Reijasse [51](-■-), Depres (●)[50], Weiss [52](-★-) and the slope at $-5/3$ (- - -) in log-log.

5. Conclusions

In this work, we investigated the performance of a dynamic mesh adaptation framework for hybrid RANS/LES simulations using high-order k-exact finite volume schemes. A refinement criterion representative of the truncation error of the reconstruction scheme was introduced and compared with heuristic criteria from the literature, showing comparable or better performance. The criterion, which naturally arises from the construction of the spatial approximation scheme, is shown to be effective for a variety of flow cases. A methodology allowing to deal with flow unsteadiness while maintaining a reasonable computational cost is also proposed. In order to deal with the solution-mesh delay problem, we used a time-average of the refinement criterion over a prespecified period, representative of the relevant time scales in the flow. Time-averaging reduces computational cost while maintaining good accuracy. To circumvent the difficulty of selecting a priori the time-averaging period, we also proposed a simple criterion to dynamically and automatically control the adaptation period. Such approach further reduces computational cost by avoiding too frequent remeshing, and avoids loss of accuracy due to too large adaptation time intervals. The strategy has proven to be effective for a realistic configuration, namely, the

compressible turbulent flow around an axysymmetric backward-facing step. Comparisons of the results with numerical and experimental studies in the literature show that the present DMA strategy resolves the relevant large-scales in the flow, allowing to capture the dominant flow frequencies. The proposed DMA framework uses a refinement criterion inherent to the present successive-correction k-exact reconstruction scheme. As a consequence, the criterion is not straightforward to adapt for different discretization schemes. On the contrary, the time-averaging approach can be applied to any other error estimator, as well as the APC criterion. We then plan to evaluate such strategies for radically different flow solvers, such as finite-element solvers or finite volume solvers employing more standard discretization schemes. Another limitation is that the present criterion is purely based on a numerical error estimator, and it does not account explicitly the amount of resolved turbulence. In future work, the present criterion could be combined with a more physics-inspired criterion such as Pope's criterion (considered in [43] or the structure function [13] to leverage the strengths of both error-based and feature-based methods.

Acknowledgments

This research work has been supported by the DGAC through the MAMBO Project. We would like to thank in particular David Puech and Jean Collinet from Arianegroup for providing FLUSEPA support and all the discussions and guidance during this research. We are also thankful to CEA (CCRT) for allocating computing time on CCRT Topaze supercomputer.

References

[1] G. Pont, P. Brenner, P. Cinnella, B. Maugars, J.-C. Robinet, Multiple-correction hybrid k-exact schemes for high-order compressible RANS-LES simulations on fully unstructured grids, Journal of Computational Physics 350 ((2017)) 45–83.

[2] P. R. Spalart, Detached-eddy simulation, Annual review of fluid mechanics 41 (2009) 181–202.

[3] S. Deck, Recent improvements in the ZDES formulation, Theoretical and Computational Fluid Dynamics 26 (2012) 523–550.

[4] P. R. Spalart, S. Deck, M. L. Shur, K. D. Squires, M. K. Strelets, A. Travin, A new version of detached-eddy simulation, resistant to ambiguous grid densities, Theoretical and computational fluid dynamics 20 (2006) 181–195.

[5] M. S. Gritskevich, A. V. Garbaruk, J. Schütze, F. R. Menter, Development of DDES and IDDES formulations for the k-ω shear stress transport model, Flow, turbulence and combustion 88 (2012) 431–449.

[6] P. Batten, U. Goldberg, S. Chakravarthy, Interfacing statistical turbulence closures with large-eddy simulation, AIAA Journal 42 (3) (2004) 485–492.

[7] S. Girimaji, K. Abdol-Hamid, Partially-averaged navier stokes model for turbulence: Implementation and validation, in: 43rd AIAA Aerospace Sciences Meeting and Exhibit, (2005), p. 502.

[8] J. Perot, J. Gadebusch, A stress transport equation model for simulating turbulence at any mesh resolution, Theoretical and Computational Fluid Dynamics 23 (2009) 271–286.

[9] C. Ollivier-Gooch, Summary of discussions of mesh impact on cfd simulations at GMGW2, AIAA Aviation Forum (2019) 17–21 June 2019, Dallas, Texas.

[10] G. Daviller, J. Dombard, G. Staffelbach, J. Herpe, D. Saucereau, Prediction of flow separation and side-loads in rocket nozzle using large-eddy simulation, International Journal of Computational Fluid Dynamics 34 (7-8) (2020) 622–632.

[11] F. Alauzet, A. Loseille, G. Olivier, Time-accurate multi-scale anisotropic mesh adaptation for unsteady flows in CFD, Journal of Computational Physics 373 (2018) 28–63.

[12] X. S. Jinlan Gou, X. Yuan, Adaptive mesh refinement method-based large eddy simulation for the flow over circular cylinder at ReD = 3900, International Journal of Computational Fluid Dynamics 32 (1) (2018) 1–18.

[13] A. Abbá, A. Recanati, M. Tugnoli, L. Bonaventura, Dynamical p-adaptivity for LES of compressible flows in a high order DG framework, Journal of Computational Physics 420 (2020) 109720.

[14] A. M. Rueda-Ramírez, G. Ntoukas, G. Rubio, E. Valero, E. Ferrer, Truncation error-based anisotropic p-adaptation for unsteady flows for high-order discontinuous galerkin methods, International Journal of Computational Fluid Dynamics 37 (6) (2023) 430–450.

[15] F. Basile, C. Jean-Baptiste, M. de la Llave Plata, R. Laraufie, P. Frey, Unstructured h- and hp-adaptive strategies for discontinuous galerkin methods based on *a posteriori* error estimation for compressible flows, Computers & Fluids 233 (2022) 105245.

[16] V. Dolejší, G. May, An Anisotropic hp-mesh Adaptation Method for Time-Dependent Problems Based on Interpolation Error Control, Journal of Scientific Computing 95 (2023).

[17] A. Jalali, C. Ollivier-Gooch, An *hp*-adaptive unstructured finite volume solver for compressible flows, Int J Numer Meth Fluids. 85 (2017) 563–582.

[18] S. Toosi, J. Larsson, Anisotropic grid-adaptation in large eddy simulations, Computers & Fluids 156 (2017) 146–161.

[19] A. Hay, M. Visonneau, Adaptive finite-volume solution of complex turbulent flows, Computers & Fluids 36 (2007) 1347–1363.

[20] J. Wackers, G. Deng, A. Leroyer, P. Queutey, M. Visonneau, Adaptive grid refinement for hydrodynamic flows, Computers & Fluids 55 (2012) 85–100.

[21] F. Alauzet, L. Frazza, Feature-based and goal-oriented anisotropic mesh adaptation for RANS applications in aeronautics and aerospace, Journal of Computational Physics 439 (2021) 110340.

[22] T. Coupez, Metric construction by length distribution tensor and edge based error for anisotropic adaptive meshing, Journal of Computational Physics 230 (2011) 2391–2405.

[23] Z. Xiao, C. Ollivier-Gooch, J. D. Zuniga Vazquez, Anisotropic tetrahedral mesh adaptation with improved metric alignment and orthogonality, Computer-Aided Design 143 (2022) 103136.

[24] L. Remaki, W. Habashi, Pacing CFD: automatic mesh adaptation as an efficient tool to improve CFD accuracy, International Journal of Computational Fluid Dynamics 19 (8) (2005) 571–580.

[25] X. Zhao, R. Conley, N. Ray, V. S. Mahadevan, X. Jiao, Conformal and non-conformal adaptive mesh refinement with hierarchical array-based half-facet data structures, Procedia Engineering 124 (2015) 304–316.

[26] N. M. Chaderjian, Advances in rotor performance and turbulent wake simulation using des and adaptive mesh refinement, in: 7^{th} International Conference on Computational Fluid Dynamics (ICCFD7), no. ARC-E-DAA-TN5574, (2012).

[27] O. Antepara, O. Lehmkuhl, R. Borrell, J. Chiva, A. Oliva, Parallel adaptive mesh refinement for large-eddy simulations of turbulent flows, Computers & Fluids 110 (2015) 48–61.

[28] J. Wackers, G. Deng, E. Guilmineau, A. Leroyer, P. Queutey, M. Visonneau, Combined refinement criteria for anisotropic grid refinement in free-surface flow simulation, Computers & Fluids 92 (2014) 209–222.

[29] A. Belme, A. Dervieux, F. Alauzet, Time accurate anisotropic goal-oriented mesh adaptation for unsteady flows, Journal of Computational Physics 231 (19) (2012) 6323–6348.

[30] M. Sharbatdar, C. Ollivier-Gooch, Mesh adaptation using C^1 interpolation of the solution in an unstructured finite volume solver, Int J Numer Meth Fluids. 86 (2018) 637–654.

[31] T. R. Michal, F. Alauzet, A. Loseille, L. Frazza, D. L. Marcum, D. S. Kamenetskiy, Comparing anisotropic error estimates for the onera M6 wing RANS simulations, in: 2018 AIAA Aerospace Sciences Meeting, (2018), p. 0920.

[32] I. Celik, M. Klein, M. Freitag, J. Janicka, Assessment measures for URANS/DES/LES: an overview with applications, Journal of Turbulence 7 (2006).

[33] X. Gloerfelt, P. Cinnella, Large eddy simulation requirements for the flow over periodic hills, Flow, Turbulence and Combustion 103 (2019) 55–91.

[34] S. B. Pope, Turbulent Flows, Cambridge University Press, (2000).

[35] S. Reuß, T. Knopp, A. Probst, M. Orlt, Assessment of local LES-resolution sensors for hybrid RANS/LES simulations, in: Progress in Hybrid RANS-LES Modelling, Vol. 130 of Notes on Numerical Fluid Mechanics and Multidisciplinary Design, Springer, (2015), pp. 93–103.

[36] P. Benard, G. Balarac, V. Moureau, C. Dobrzynski, G. Lartigue, Y. d'Angelo, Mesh adaptation for large-eddy simulations in complex geometries, Int J Numer Meth Fluids. 81 (12) (2016) 719–740.

[37] F. Haider, P. Brenner, B. Courbet, J. P. Croisille, Efficient implementation of high order reconstruction in finite volume methods, Finite Volumes for Complex Application VI-Problem & Perspectives, Springer Proceedings in Mathematics 4 ((2011)) 553–560.

[38] P. Brenner, Unsteady flows about bodies in relative motion, 1st AFOSR Conference on Dynamic Motion CFD Proceedings, Rutgers University, New Jersey, USA, (1996).

[39] P. Brenner, Three-dimensional aerodynamics with moving bodies applied to solid propellant, in: 27th Joint Propulsion Conference, (1991), p. 2304.

[40] A. Limare, P. Brenner, H. Borouchaki, An adaptive remeshing strategy for unsteady aerodynamics applications, in: 46th AIAA Fluid Dynamics Conference, (2016), p. 3180.

[41] A. Limare, Raffinement adaptatif de maillages intersectants en volumes finis d'ordre élevé pour l'aéropropulsion, Ph.D. thesis, Université de Technologie de Troyes (2017).

[42] F. Ducros, V. Ferrand, F. Nicoud, C. Weber, D. Darracq, Large eddy simulation of the shock/turbulence interaction, Journal of Computational Physics 152 (1999) 517–549.

[43] A. Limare, H. Borouchaki, P. Brenner, Adaptive mesh refinement with an automatic hybrid RANS/LES strategy and overset grids, in: Progress in Hybrid RANS-LES Modelling: 7th Symposium on Hybrid RANS-LES Methods, 17–19 September, Berlin, Germany, Springer, (2018), pp. 159–168.

[44] S. Ghosal, P. Moin, The basic equations for the large eddy simulation of turbulent flows in complex geometry, Journal of Computational Physics 118 (1) (1995) 24–37.

[45] U. Piomelli, S. Kang, F. Ham, G. Iaccarino, Effect of discontinuous filter width in large-eddy simulations of plane channel flow, Proceedings of the Summer Program 2006 (2006) 151–162.

[46] L. Goodfriend, F. K. Chow, M. Vanella, E. Balaras, Large-eddy simulation of decaying isotropic turbulence across a grid refinement interface using explicit filtering and reconstruction, Journal of Turbulence 14 (12) (2013) 58–76.

[47] S. Mozaffari, E. Guilmineau, M. Visonneau, J. Wackers, Average-based mesh adaptation for hybrid RANS/LES simulation of complex flows, Computers & Fluids 232 (2022) 105202.

[48] H. Yee, M. Vinokur, M. Djomehri, Entropy splitting and numerical dissipation, Journal of Computational Physics 162 (1) (2000) 33–81.

[49] N. Sandham, H. C. Yee, A numerical study of a class of TVD schemes for compressible mixing layers, Tech. rep. (1989).

[50] D. Deprés, P. Reijasse, J. Dussauge, Analysis of unsteadiness in afterbody transonic flows, AIAA journal 42 (12) (2004) 2541–2550.

[51] P. Meliga, P. Reijasse, Unsteady transonic flow behind an axisymmetric afterbody equipped with two boosters, in: 25th AIAA applied aerodynamics conference, (2007).

[52] P.-É. Weiss, S. Deck, J.-C. Robinet, P. Sagaut, On the dynamics of axisymmetric turbulent separating/reattaching flows, Physics of Fluids 21 (7) (2009).

[53] D. Mabey, R. A. Establishment, Pressure Fluctuations Caused by Separated Bubble Flows at Subsonic Speeds, ARC 33145, RAE, 1971.

[54] I. Lee, H. J. Sung, Characteristics of wall pressure fluctuations in separated and reattaching flows over a backward-facing step : Part (I) Time-mean statistics and cross-spectral analyses, Experiments in Fluids 30 (3) (2001) 262–272.

[55] D. M. Driver, H. L. Seegmiller, J. G. Marvin, Time-dependent behavior of a reattaching shear layer, AIAA journal 25 (7) (1987) 914–919.